# Manufacturing and Characterization of Welded, Sintered Condensers for a Loop Heat Pipe

by

Jay D Sircar

Submitted to the
Department of Mechanical Engineering
in Partial Fulfillment of the Requirements for the Degree of

Bachelor of Science in Mechanical Engineering

at the

Massachusetts Institute of Technology

June 2013

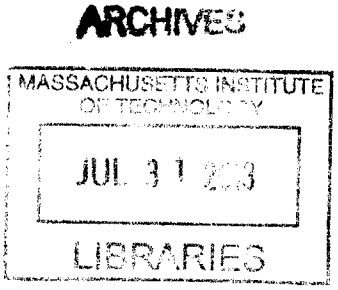




Signature of Author: _____

Department of Mechanical Engineering
May 22, 2013

Certified by: _____

Evelyn N. Wang
Associate Professor of Mechanical Engineering
Thesis Supervisor

Accepted by: _____

Anette Hosoi
Professor of Mechanical Engineering
Undergraduate Officer

# Manufacturing and Characterization of Welded, Sintered Condensers for a Loop Heat Pipe

by

Jay D Sircar

Submitted to the Department of Mechanical Engineering
on May 22, 2013 in Partial Fulfillment of the
Requirements for the Degree of

Bachelor of Science in Mechanical Engineering

## ABSTRACT

A manufacturing process plan was developed for a welded condenser utilizing a sintered wick. Electronic devices have progressed to the point where new designs are limited by the thermal management system used to ensure safe operating temperatures. Coupling the effects of high surface area of multiple condensers, the low thermal resistance of loop heat pipes, and the increased dissipation rates with an integrated fan system, a high efficiency heat exchanger has been previously designed. The multiple-condenser loop heat pipe required reliably manufactured condensers, with specified internal features composed of sinter wick material in order to prevent flooding and flash vaporization; key challenges faced by having multiple condensers in a loop heat pipe. The implementation of a functional sintered bond used to assemble the condenser and a welded flange design for the creation of a hermetic seal, resulted in a more reliable condenser, which functioned in a similar manner to previous designs. Additionally, the performance of the condenser under air restriction was addressed.

Thesis Supervisor: Evelyn N. Wang
Title: Associate Professor of Mechanical Engineering

# Acknowledgements

I would like to thank my wonderful adviser Professor Evelyn Wang for her help, advice, and support. I must also thank Daniel Hanks for being the best day-to-day supervisor one can have. His patience and guidance in all things from hands on training, to brainstorming, and to proofing my thesis, helped me successfully navigate this challenging journey. I am also grateful for the direction and leadership provided by Teresa Peters and Martin Cleary, and the general camaraderie of the PHUMP team including Arthur Kariya, Wayne Staats, and Nick Roche. Mike DeMaree, Kurt Broderick, and Don Strahan provided invaluable technical expertise and training for this project. Finally, I wish to acknowledge the Defense Advanced Research Projects Agency (DARPA) for funding the Microtechnologies for Air-Cooled Exchangers (MACE) program that supports this research.

# Contents

# List of Figures & Tables

# Chapter 1

# Introduction

Thermal management is a crucial design consideration for electronic devices. High levels of heat dissipation from computer processors, power electronic devices, and other advanced electronics, unless efficiently removed, can limit device performance [1]. Natural convection alone cannot keep up with the thermal energy generated by these computer chips, which can easily surpass $100\ W/cm^2$. Thermal management solutions strive to dissipate high thermal loads to the ambient environment. A 2007 study carried out by the Department of Energy Advanced Manufacturing Office concluded that US data centers alone used up to 120 TWhr a year [2]. On average, 63% of data center power usage goes to cooling solutions, which means for every watt used for computational work, two watts are used to remove the waste heat generated. This clearly indicates the need for more efficient heat sinks. [3]

## 1.1 Background

The compaction of electronics has resulted in a sharp rise in the heat flux in these devices [4, 5]. If the generated high heat fluxes are not removed, performance of the electronic chips may falter, and may fail to function entirely. The need for low thermal resistance and high reliability thermal management systems has led to increased research and implementation of several different systems such as liquid cooling [6] which, while effective with high heat fluxes, usually requires high pumping power, thus reducing its coefficient of performance. Liquid cooling solutions may also be prone to corrosive failures and add on complexity, cost, and size [7, 5]. Regardless of the intermediate heat transfer loops employed, ambient air is always the final heat sink [8]. However, air suffers from having low density, poor thermal conductivity, and low specific heat, which limits the convective heat transfer coefficient to the order of

$50\ ^{W}/_{m^2K}$ [9]. The Defense Advanced Research Projects Agency Program on Microtechnologies for Air-Cooled Exchanger is working towards increasing the performance of air-cooled heat exchangers, while reducing their size and weight, by using advanced technologies.

## 1.2 Description of the System

In order to take advantage of air cooling, the area of heat transfer is increased through the use of fins [9]. Fins are typically made of low cost, high thermal conductivity metals such as copper or aluminum. Forcing the flow over the fins helps increase the heat transfer. Fins are most efficient when the overall surface temperature is as high as possible. Fin efficiency is improved by maximizing the heat spread throughout the exchanger. Loop heat pipes have been used for this purpose.

Loop heat pipes (LHP) are passive two-phase heat transport devices that operate on a closed cycle [4]. The marked improvement in heat transfer within LHP over solid fins is due to the fact that they employ phase change heat transfer, which has heat transfer coefficients as high as $100\ ^{kW}/_{m^2K}$. This provides very low thermal resistance during heat transport and allows the surface area of the condenser to be nearly isothermal, and thus, not suffer from lower fin efficiencies seen with solid fins [4, 10]. Although LHPs are not designed to have parallel condensations pathways, the MIT Pumped Heat Exchanger (device referred to as PHUMP) team, designed and prototyped a multi-condenser LHP which utilizes sinter wick in the condensers themselves [6, 11]. The sinter within the condenser allows for a stable liquid-vapor interface which prevents the lower condensers from flooding due to the gravity-induced pressure of the top layers' condensate.

The PHUMP was designed to dissipate 1000 W from a heat source at 80 °C to ambient air at 30 °C using no more than 33 W of electrical input to drive forced convection [6]. A comparison of PHUMP target

performance and current state-of-the-art air-cooled solution metrics are presented in Table 1 for operation at 1000 W heat dissipation:

| | Current air-cooled solutions [7] | PHUMP [6] |
|---|---|---|
| Working temperature differential [K] | 200 | **50** |
| Overall thermal resistance $[^{K}/_{W}]$ | 0.2 | **0.05** |
| Coefficient of Performance [ ] | 10 | **30** |

**Table 1- Current air-cooled heat exchanger and PHUMP target performance metrics**

To meet the DARPA requirement for weight and size improvements in air cooling, the PHUMP was designed to be contained within a 10 cm x 10 cm x 10 cm cube, and for versatility be able to operate in any orientation.

A schematic diagram of the overall PUMHP design is shown in Figure 1. The single evaporator at the base receives the waste heat from a variety of sources. Above the evaporator are alternating layers of condensers and impeller blades (with adequate gap spacing). A low-profile three-phase radial-flux permanent-magnet synchronous motor is mounted on top of the device [12]. Air inlets above the motor allow for cooler ambient air to enter the core of the heat exchanger, with impellers driving the air radially outward over and under the condenser faces. The impellers have been optimized to 1.5 mm thickness with a 0.5 mm gap spacing on either side to the condenser [13]. This impeller configuration has high convective heat transfer coefficients due to the shearing of the momentum and thermal boundary layers that form on the condensers. This design has been shown to result in near isothermal conditions between the evaporator and condensers (~5°C) [6].

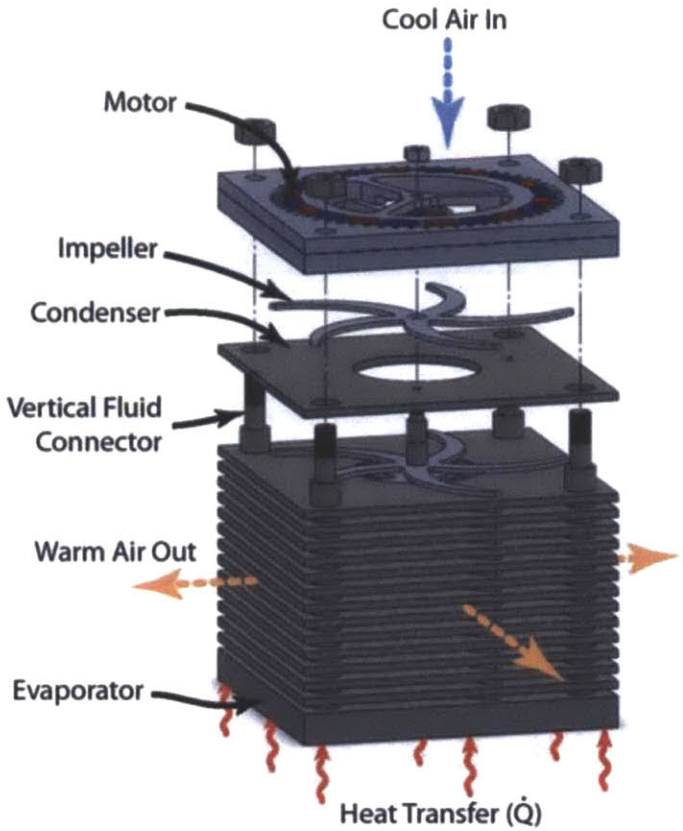


**Figure 1- Schematic diagram of an integrated fan heat sink**

The pumped heat exchanger (PHUMP) consists of a series of centrifugal fans operating in parallel to cool the condensers of a loop heat pipe. The heated surface on the bottom is the evaporator of the heat pipe. A compact motor at the top of the device drives impellers interdigitated between the condensers. (Reproduced with permission from Hanks [6])

Figure 2 depicts the basic functionality of a multi-condenser LHP. The evaporator receives heat input from conduction, which is used to vaporize the working fluid. Water was chosen as the working fluid due to its high latent heat of vaporization and relative ease of handling. Vapor generated leaves the evaporator though the vapor lines. As shown in Figure 1, there are a total of four fluid lines- two vapor and two liquids. Vapor, indicated by the red line, travels towards the different condensers and cools into liquid as heat is transferred through the condenser walls to the surrounding ambient air. The liquid travels through the porous sinter in the subcooling channel, which separated the vapor, allows the liquid to cool down from saturation. Once water reaches the wick-free liquid lines, shown as solid blue, it flows back down to the evaporator, and the cycle continues.

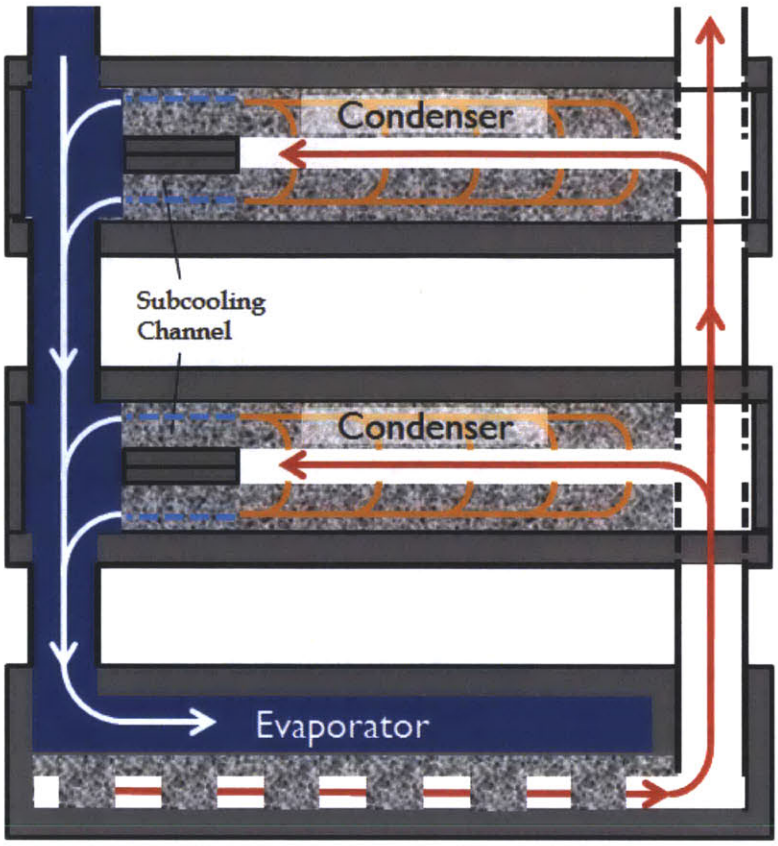


**Figure 2- Example flow cycle for the multi-condenser loop heat pipe**
The simplified schematic diagram shows the internal heat pipe structure (Reproduced with permission from Hanks [6]).

Multiple condensers introduce the possibility for flooding which could prevent the working cycle from continuing. The gravitational pressure head of water in the top condensers might be sufficient to force liquid to displace vapor in the lower condensers. The 10 cm height is equivalent to roughly 1 kPa of hydrostatic pressure. Additionally, the design requirement for position versatility would not be met if the condenser furthest from the evaporator floods with liquid when inverted. These concerns are addressed with the addition of wicking material in the condenser. The liquid-vapor interface is stabilized by capillary forces generated by the surface tension between the water and the sinter particles [6, 4]. The meniscus that forms between the two phases is then a function of the surface wettability, liquid surface tension, pore size of the sintered wick, and pressure difference between the two phases. The most dynamic property of the operational setup is the differential pressure. The rest of the properties are

relatively static and contribute to $\Delta P_{cap,max}$. This value is the pressure difference between the vapor and liquid phases when the meniscus fails and vapor is able to penetrate into the region of the liquid phase, as depicted in Figure 3.

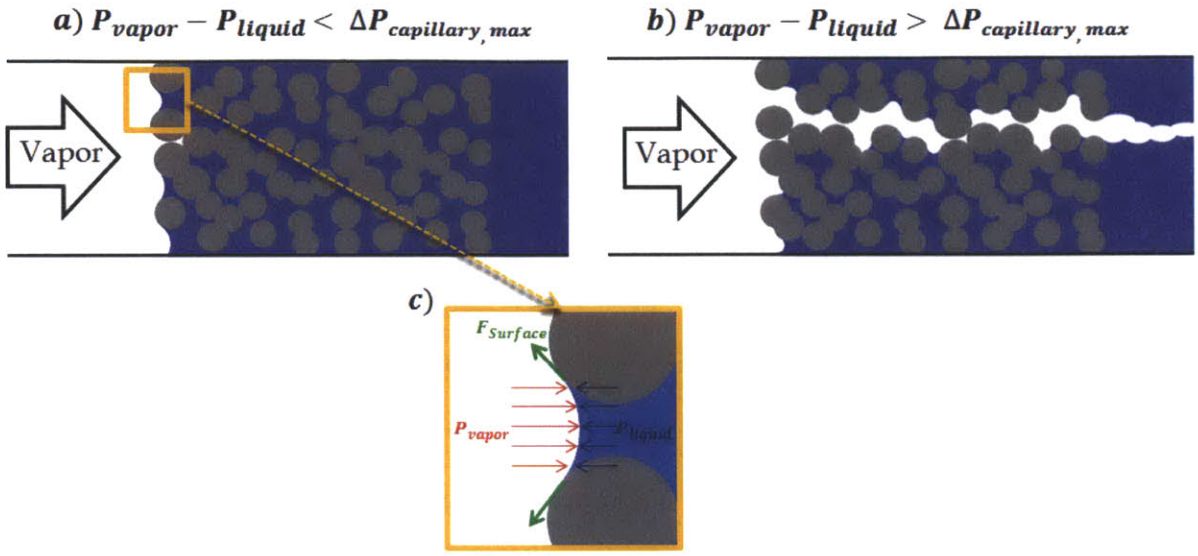


**Figure 3- Schematic diagram depicting the effect of differential pressure in capillary porous beds**
Within the sinter, pressures of the two phases determined the performance of the condenser. (a) During stable operation the vapor pressure is balanced by both the liquid pressure and the pressure needed to overcome the wick pressure drop, (b) during breakthrough failure, the differential pressure is high enough to overcome the maximum capillary pressure throught the wick, (c) enlargment at the vapor-liquid interface shows a force blance and the resulting meniscus (adapted with permission from Hanks [5])

## 1.3 Literature Review

The PHUMP team has previously designed and manufactured a multiple- condenser loop heat pipe using porous sintered condensers to stabilize the liquid phase. Multiple modules and proof-of concept tests were carried out and design criteria optimized. Design work included the 3-D resister modeling of the overall system [14], motor and impeller performance modeling [13], and finite element analysis of the individual components of the PHUMP [15, 16, 6]. Experiments were carried out to: determine thermal properties of the different sinters in order to aid in the selection of the sinter material and particle size [17], determine the sub-cooling length needed to mitigate the failures associated with multiple-condensers

[18], characterize separately the performance of the evaporator, of a single condenser, of multiple parallel condensers [15, 11, 6], and of various impeller blades [13]. System level tests were carried out for single and multiple condenser heat exchangers [19]. This work has been expanded in the present thesis in two aspects: first, with a new design for fabrication based on welding condensers and second, by determining the effects of air restriction on single-condenser performance.

## 1.4 Thesis Overview

The focus of this thesis was to come up with a new process plan for fabricating condensers with sintered wicks for a loop heat pipe heat exchanger. The performance of the new condensers was compared to the performance of the original design. Chapter 1 introduces the necessity for a multi-condenser loop heat pipe, operational challenges, and the designed solutions developed earlier by the PHUMP team. Chapter 2 describes the operation of the looped heat pipe, detailing the process plan previously implemented in the condenser fabrication. Chapter 3 details the development of the new process plan for condenser fabrication. Chapter 4 provides the experimental analyses that were previously designed to characterize condensers and the experimental procedure used to restrict airflow over the condenser. Finally, Chapter 5 concludes with recommendations for future work.

# Chapter 2

# Design Requirements & Original Fabrication Plan for Sintered Condensers

## 2.1 Requirements

A condenser was designed to meet the specific thermo-fluidic requirement to function properly in a multi-condenser LHP heat exchanger. Due to the reduced operating pressures within the system compared to the atmosphere, and because of the need to maintain pure water as working fluid, the condenser must be manufactured with all joints hermetically sealed with a maximum helium leak rate of $10^{-9}$sccm .

### 2.1.1 Capillary Pressure

As described in Section 1.3, a higher breakthrough pressure $\Delta P_{cap,max}$, in the sintered wick is required to better stabilize the liquid-vapor interface. According to the Young-Laplace Equation, the maximum capillary pressure can be defined as:

$$\Delta P_{cap,max} = \frac{2\sigma \cos\theta}{d_p} \tag{1}$$

where $d_p$ is the pore diameter, $\sigma$ is the surface tension, and $\theta$ is the contract angle between the liquid and the sinter particle surface. The pore diameter $d_p$ cannot be decreased indefinitely due to the pressure drop generated throughout the passively driven cycle. Darcy's Law defines the pressure drop of a fluid flowing through a porous medium as:

$$\Delta P = \frac{\mu \dot{V} L}{\kappa A} \tag{2}$$

where $\mu$ is the viscosity of the fluid, $\dot{V}$ is the volumetric flow rate, L is the flow distance, $\kappa$ is the permeability of the wick, and A is the cross-sectional area of the wick. The permeability of the wick is proportional to the pore diameter as per:

$$\kappa \propto \frac{1}{d_p^2} \tag{3}$$

As demonstrated in Figure 3(b) if $\Delta P_{cap,max}$ is too small, vapor will break into the liquid region. This can plug the liquid tubes and prevent liquid from flowing down to the evaporator. This in turn can cause the evaporator to critically overheat. If the $\Delta P_{cap,max}$, is too large then the viscous pressure drop associated with the fluid flowing through the wick will be large and the flow resistance will be too large for the condensing liquid to reach the evaporator. The optimized properties of the evaporator with maximum allowed operating temperature set-point of 100 °C require that the maximum breakthrough pressure of each of the condensers be greater than 6 kPa [6].

### 2.1.2 Subcooling

Condensate entering the liquid lines can spontaneously evaporate if it exits the wick at saturation temperature. Similar to vapor breakthrough, spontaneous evaporation can also plug the cycle. The subcooling length of each condenser depicted in Figure 2 acts as a temperature buffer that prevents vaporization in the liquid return line [6]. Saturation temperature is maintained whenever the liquid and vapor phase are in contact. The physical barrier between the vapor and liquid regions allows the liquid condensate to cool below saturation due to the continued heat loss through to the condenser outer surfaces, which behaves as a fin. Figure 4(a) demonstrates the general temperature changes that occur within the symmetric half of a condenser, where red lines show the path of water vapor, and light-to-dark blue line signify condensation and subcooled water on its return to the evaporator. Figure 4(b) presents the cross-section of a single condenser from the dashed line marked AA'. Length of the subcooling

section and that of the liquid channel were optimized from previous COMSOL modeling - with a target temperature of liquid leaving the condensers being 12.6 °C cooler than the saturation temperature [20].

### 2.1.3 Material Selection

The case material for the PHUMP has to be chemically compatible with $H_2O$. Over time, most common materials such as stainless steel and aluminum alloys undergo redox reactions with $H_2O$ forming $H_2$[21]. As a non-condensable gas, hydrogen inhibits the heat transfer from a heat pipe by the creation of a gas plug, and increases thermal resistance created by stationary pockets of gases at nucleation sites [6]. Gold, silver, copper, and a copper alloy, Monel 400, have been shown to be unreactive to pure water. For economic reasons, Monel and copper were used as materials to manufacture PHUMP components directly in contact with the working fluid.

The sinter wick material was selected by a similar chemical compatibility assessment. A previous study calculated the particle material, diameter, and geometry that provided the best combination for permeability, breakthrough pressure, and thermal conductivity for multiple-condenser LHPs [17]. For the condenser wick, 44 μm non-spherical Monel powder was selected.

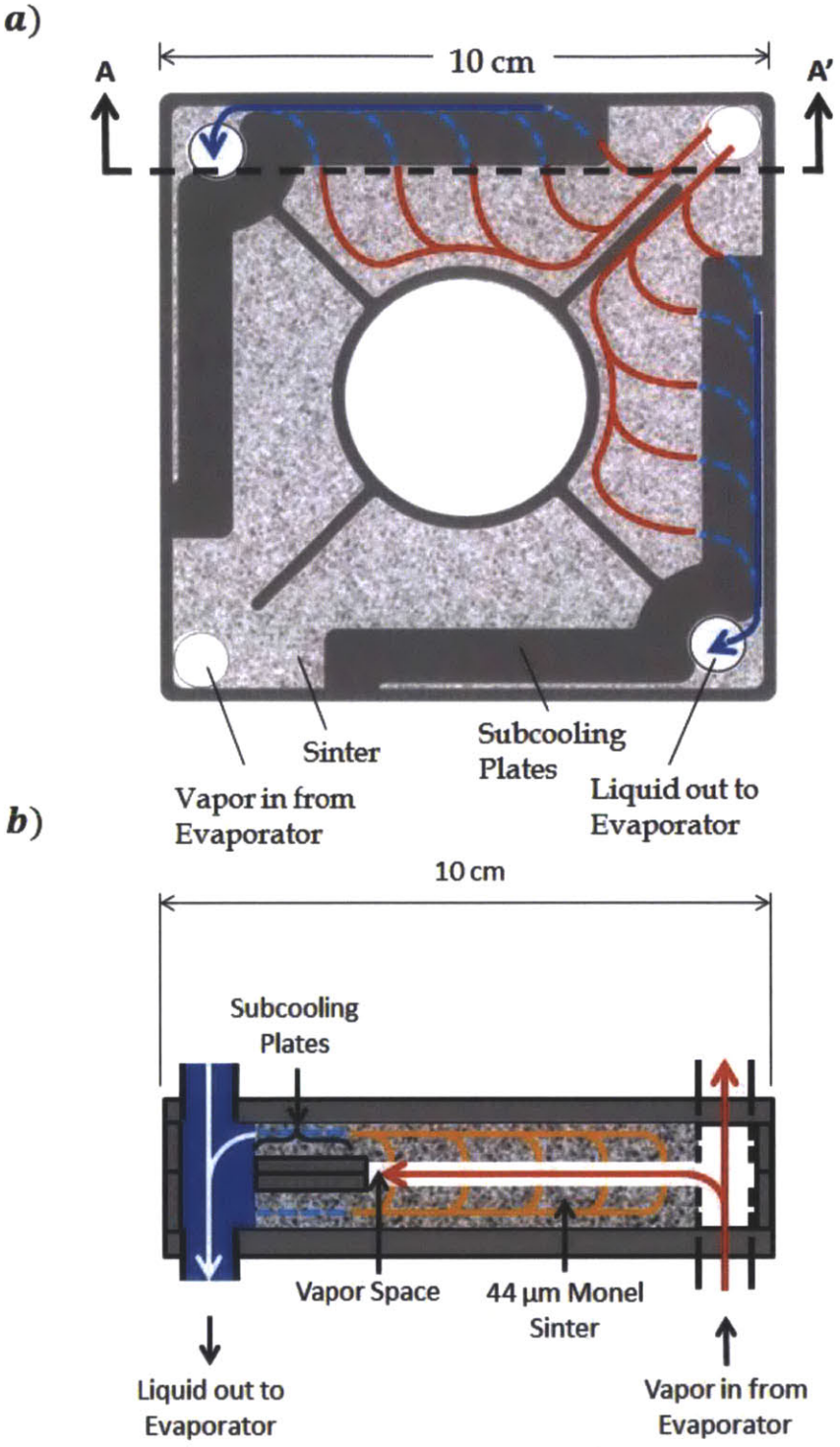


**Figure 4- Schematic diagram of vapor and liquid pathways inside a brazed condenser**

(a) Top view of a half condenser reveals the internal structures of a sintered LHP condenser. Vapor enters the condenser and is cooled to liquid by the time it reaches the subcooling plates, where it loses sensible heat during stable operation. (b) Cross section **AA'** of the condenser shows the importance of the vapor gap and the sinter's role as wicking material (not to scale); the vapor gap increased the interfacial boundary area, where condensation occurs (Reproduced with permission from Hanks [6]).

## 2.2 Alpha Condenser

The original condenser fabrication process plan required steps. The first involved brazing the base plate to the internal frame piece. This formed half of the condenser. The second step was to fill in a sinter wick within the condenser halves. The final step involved brazing the two halves together.

### 2.2.1 Original Process Plan

Each seal and joint for the LHP needed to be hermetically sealed, in order to prevent the buildup of non-condensable gases, loss of the working fluid, or promotion of corrosion. System assembly-ready condensers were tested using a helium leak detector to ensure there would be no appreciable changes to the working fluid within the closed LHP cycle. In order to maintain near isothermal conditions close to the applied temperature at the evaporator, wall conduction resistances had to be minimized, which resulted in the usage of thin walled condensers and tubes. Finally, due to the requirement for impeller blades to be able to shear away the fluid boundary layers, tolerances for thickness and alignment had to be very high. The process plan that was developed for brazed condensers has been described in detail by Hanks [6: Section 2.2].

For the original design, a frame and a base plate piece were photo-chemically etched from sheets of Monel 400 using a high precision process (Photofabrication Engineering Inc., Milford, MA). The frame plate, as shown in Figure 5-(a), divided the condenser into separate regions (vapor, sub-cooling, liquid), and also provided structural support by properly spacing out the two halves of the condensers and ensuring the presence of a vapor gap which increased the surface area between the vapor and the condensed liquid filled, porous structure. For the first joining procedure, a pure silver braze with a melt temperature of 970 °C was used. Each half condenser was then centrifugally packed with 44 μm non-spherical Monel powder. The Monel particles in the vapor region were then scrapped away to create a total vapor gap of 0.5 mm thickness. A short transition region of sinter remained as shown in Figure 5(b),

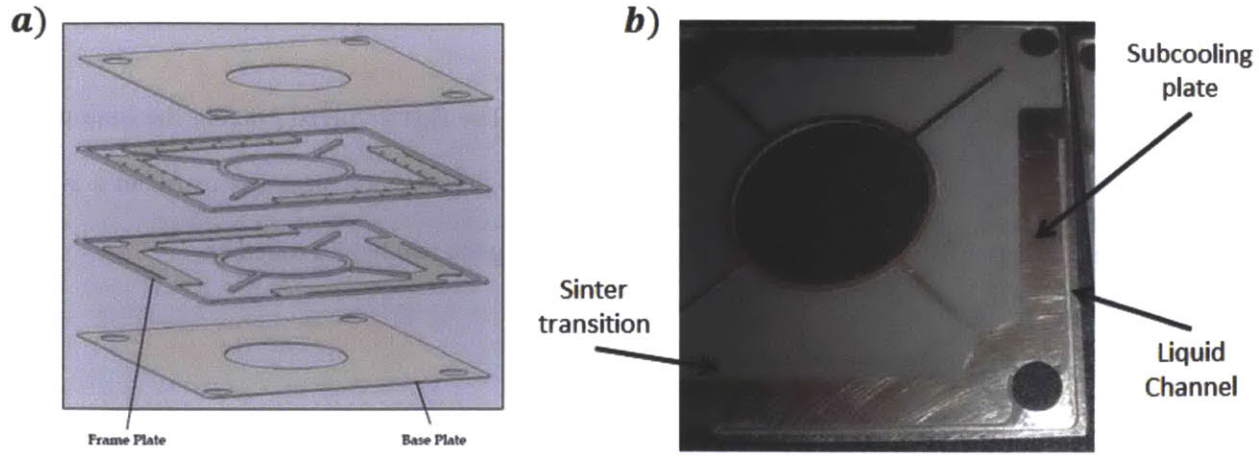


**Figure 5- Process plan for brazed condensers**

a) Exploded view of the four solid pieces used in each brazed condenser. After each pair of frame and base plate were joined, the half condensers were spin-packed with Monel particles and were sintered to form the wick (Reproduced with permission from Hanks [6]). (b) The vapor gap was carved out before the sintering, and the liquid channel was carved out later. The sinter transition was put in to ensure that any shrinkage under the subcooling plate did not allow the vapor direct acces to the liquid channel. The subcooling plates were lustrous due to the a fine sanding that was used to clean and prepare the surface for the next braze step that joined the two halves togther.

in order to mitigate the likelihood of high permeability regions forming under the subcooling plate due to linear contraction during the sinter process. This transition also aided in ensuring that the vapor did not have access to the liquid channel after passing through un-wicked gaps that may have formed between the subcooling plates when the halves are assembled together. This first application of Monel particles was sintered at 820 °C for 12 mins. Since linear shrinkage could be as large as 15% leaving regions of high permeability, fresh Monel powder was added to compensate for such shrinkage before the condenser halves were re-sintered at 820 °C [17, 6]. After each sinter process, the liquid channel depicted in Figure 5(b) was carved out. This length reduced the barrier for sub-cooled liquid returning to the evaporator, and ensured that the pressure drop from the vapor to liquid lines did not become too great to result in flooding of the condenser. Since the frame and the base plate were brazed at a higher temperature than the sintering process, the two condenser halves could not be joined using the same pure silver braze. A lower temperature eutectic AgCu (72% Ag, 28% Cu) with a melt temperature of 810 °C was used.

To ensure that the completed LHP could operate at least up to 100 °C, condensers were tested for capillary breakthrough pressures in excess of 6 kPa. Air was used as a substitute for vapor, and the condensers were flooded with distilled water. Positive pressure was applied and gradually increased at single vapor inlets until the meniscus failed and air was able to bubble out of an adjacent liquid channel (see Figure 6). All four combinations of vapor inlets and liquid outlets were tested. The minimum value was recorded as $\Delta P_{cap,max}$. Suitable condensers were first tested for proper sealing by submerging them under water with all ports sealed, and held at positive pressure to detect macroscopic leaks. Microscopic leak detection tests were performed with a helium leak detector.

Brazing the condenser was not an optimal solution for joining the sintered condenser halves. The AgCu braze was prone to wicking into the sinter, generating leaks and clogging the porous structure. Also, the lower temperature AgCu braze did not wet as well on Monel as did the pure Ag braze. The capillary action that formed the brazed bond required very close contact (~25 μm). Leaks were sealed with vacuum grade epoxy (Torr Seal, Varian Vacuum Technologies) (shown in Figure 6); epoxy is brittle and not reliable given the thermal stresses during the service life of the LHP.

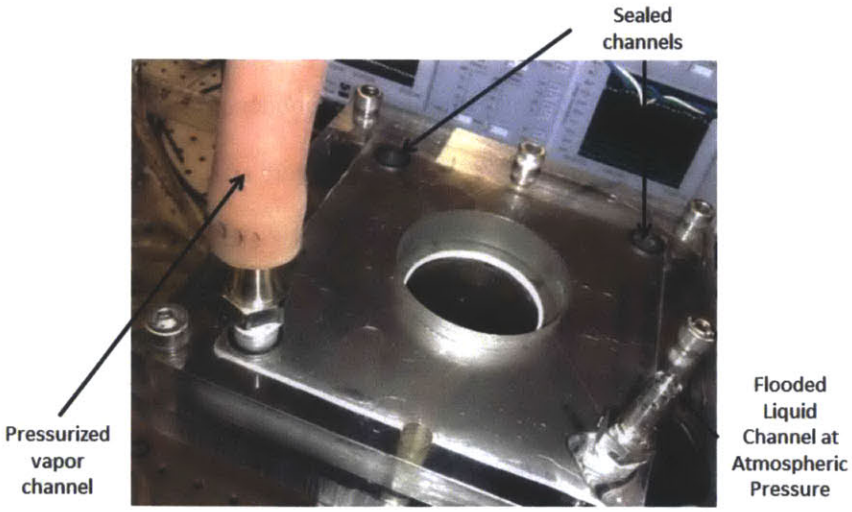


**Figure 6- Quality check for the completed brazed condenser**

Each brazed, expoy-sealed condenser was tested to ensure that that it was leak-tight and had a suitable capillary breakthrough pressure. A syringe pump (not shown) compressed air into each vapor channel, thereby building up pressure. An adjacent liquid channel was left open. The presence of bubbles indicated that the pressure generated surpased the caillary breakthrough pressure of the condenser. Capping the liquid line and pressurizing the entire condenser under water ensured that there were no major leaks.

# Chapter 3

# Manufacturing Iterations for Beta Condensers

The need for functional, reliable, hermetically sealed sintered condensers with high tolerances prompted investigating two alternative manufacturing processes. One process was based on chemically dissolving a spacer used to create the voids between the vapor gap and the liquid channel. The other procedure was to switch from brazing to welding.

## 3.1 "Lost Mould" Silicon Spacer

Due to the fact that the success rate of pure Ag brazing Monel is high, a process plan which involved creating the entire solid condenser shell in the initial step was investigated. The key challenge was to determine whether or not internal features could be replicated after the body shell was formed. Figure 7 depicts a cross-sectional schematic of the "lost mould" process plan.

The first step was to braze together the top and bottom of the condensers with a piece of silicon fixed in the location of the vapor gap. The pegs holding up the silicon were staggered two dimensionally in order not to excessively disrupt the flow path of the condensate. Monel particles were then used to fill all empty spaces, and they were then sintered in place. Finally, the silicon was removed by dissolving it in potassium hydroxide ( KOH).

Two tests were conducted to check for validity of this approach. For the first step, the silicon presence during the braze process was examined on a test sample of sandwiched Monel plates loaded with spacers and a piece of silicon wafer that was brought up to the brazing temperature of silver. For the final step, the dissolution of silicon through a porous structure was investigated.

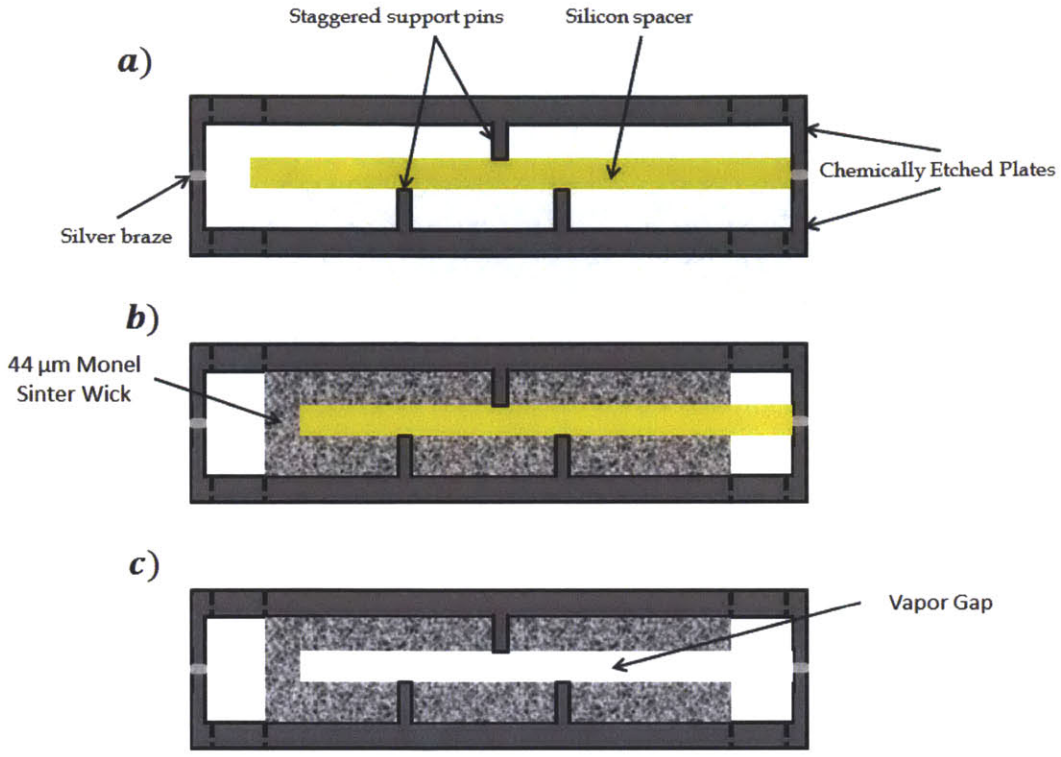


**Figure 7- Proposed process plan for a "lost mould" condenser**

a) A hollow condenser is brazed to a fixed-in-place silicon waffer with the dimensions of the desired vapor channel. (b) Monel particles then fill and pack the remaing voids within the hollow shell, and are sintered to form a single continous wick structure. (b) Using commericaly available etchants the silicon wafer is then dissolved out of the condenser leaving a vapor gap. The vapor gap and the liquid lines are sepereated by a sinter barrier to ensure subcooling.

Figure 8 presents results from the first test. At temperatures of over 1,400°C, Monel is known to form a eutectic alloy with silicon [22]. However, at the 970 °C silver braze temperature, the silicon and Monel reacted to form a very brittle alloy due to enhancement of diffusion at that temperature.

The silicon etching experiments were carried out by gently flushing warm (60°C), 20% KOH solution down a pipe plugged with sinter wick. To determine whether the chemical process would affect performance of the sinter, breakthrough capillary pressure of the sinter was measured. Results are shown in Table 2. Exposure to KOH appeared to lower the $\Delta P_{cap,max}$, and exposure to silicon etching products further lowered the maximum capillary pressure within the sinter. Qualitatively, the high viscosity of the etching products seemed to clog up the porous wick. Even if the silicon/Monel

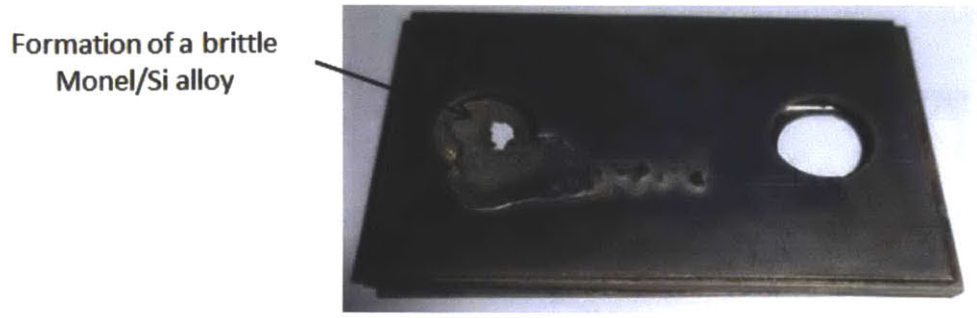


**Figure 8- Sample representing an inadvertant alloying of silicon and Monel at brazing temperatures**
A failed proof-of-concept study showing the effects of raising silicon to the required brazing temperature in the presence of silicon.

alloying could be prevented, it is unlikely that the process plan shown in Figure 7 could be carried out without significant contamination of the sinter wick.

The "lost mould" silicon spacer process was not feasible due to the chemical reactivity between Monel and silicon, and due the reduction of $\Delta P_{cap,max}$ and from chemical alteration of surface tension forces.

| Average drop in capillary pressure after: | |
|---|---|
| **Exposure to KOH** | $1.7 \pm 0.9$ kPa |
| **Silicon etching** | $3.7 \pm 1.4$ kPa |

**Table 2- Effects of silicon etching on breakthrough capillary pressure**

## 3.2 Welding with a Sinter Bridge

Welding all the joints was considered due to its wide spread use to form hermetic seals. Welding dissimilar metals can compromise the overall quality of a joint; therefore, using brazing in any of the steps was no longer an option. Sinter bridging the two condenser halves together was investigated.

### 3.2.1 Proof of Concept

The sinter in the original condenser performed no structural function. In order to establish how to use a second sintering step to create a mechanical bond (shown in Figure 9), two different test samples (depicted in Figure 10) were created, to measure the maximum capillary breakthrough pressure through the sinter bridge. The actual mechanical yield and shear strengths were not analyzed, because although the sinter bridge had to hold the two halves together, it only had to do so until the pieces were welded together.

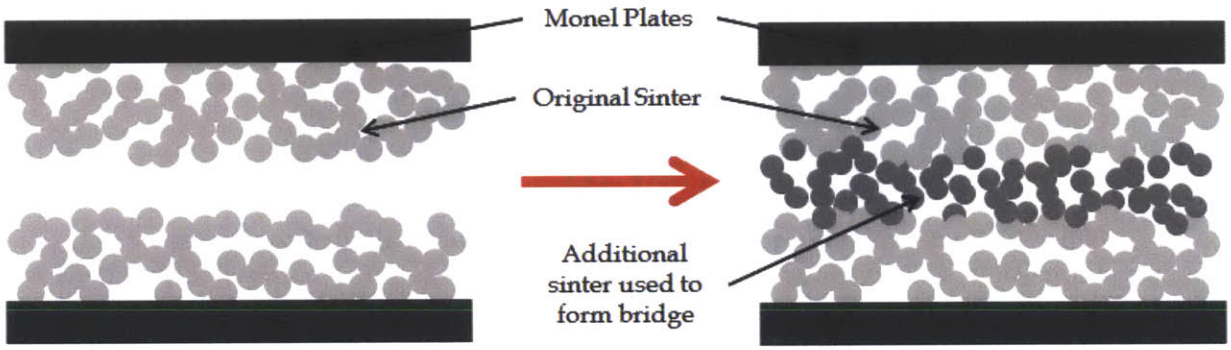


**Figure 9- Schematic diagram of a sinter bridge**

The sinter bridge was created by adding additional particles (darker gray) that were capable of sintering to each other as well as to the previously formed wick (lighter gray). Addition of the bridge should not change the pore diameter and permeability of the original wick.

The sinter bridge mainly functioned to replace the subcooling plate, which was located on the frame piece in the previous design. Uneven bonding under this plate, due to shrinkage, created highly permeable pathways thus lowering the breakthrough capillary pressure, which required the sinter transition, shown in Figure 5. Care was used to ensure that the added bridging sinter was in contact with both original wicks.

One set of samples, shown in Figure 10(a), was fabricated using flat Monel sheet metal and with uniform layer of 44 μm Monel sinter. They were assembled together using an additional thin layer of 44 μm Monel sinter heated to the same temperature as the first sinter. This process mimicked the two sinter runs used in the original condenser but relied on the second sinter step, used previously to compensate for shrinkage, to join the two different wicks. These samples came apart quite easily - simply from the shear

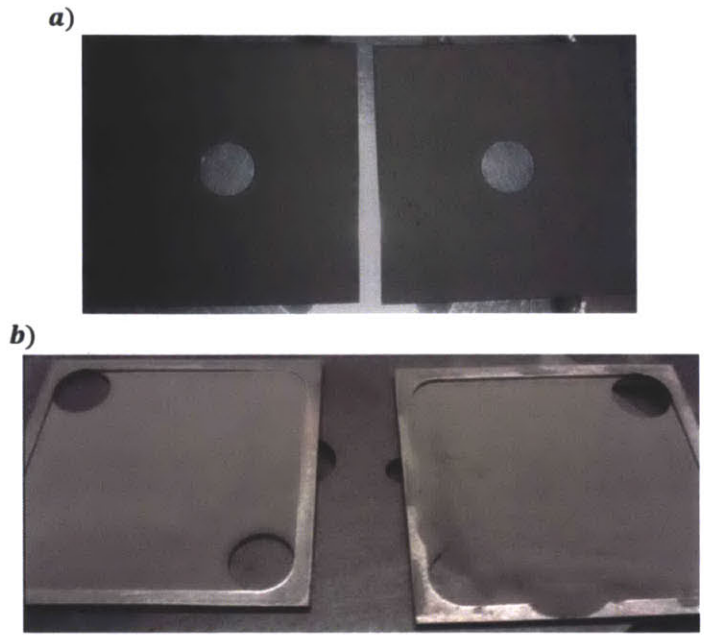


**Figure 10- Test samples used for demonstrating the weldability of condensers**

Welding samples required a sinter bridge between the two condenser halves. This ensured that there was subcooling of liquds which was esential to stably operate multiple stacked condensers. (a) intial samples simply tested the ability of a new sinter to hold the two sintered plates together, and (b) latter trials looked at the effects of selective location sinter-bridging and the capillary changes associated with the thermal expansion and contraction on the welding process.

forces that were generated when being picked up or transported.

In order to create a strong and uniform bond, the temperature of the second sinter step could be increased. This, however, would alter the optimized permeability in the bulk of the sinter wick previously formed. Instead, the particle size of the sinter used in the second step was reduced so that, at the same temperature, the smaller particles could sinter faster and create a better bond. Samples depicted in Figure 10(b), utilized 22 μm Monel sinter which was applied in a single "L" shaped sub-cooling pattern. Condenser halves were scaled down and machined out of a 0.125" Monel sheet stock. Bubble-test capillary pressures were calculated for the miniature condenser, with samples reaching $\Delta P_{cap,max}$ values as high as 4 kPa. The asymmetry of having only one subcooling channel in one corner was determined to be responsible for constraining the capillary pressure to 4 kPa, therefore further testing and optimization was

carried out for full sized condensers. Fixtures were developed to align, hold, and compress the condenser halves together during the sintering bridging step. Welding of the miniature test condensers showed slight decreases in $\Delta P_{cap,max}$, under 1 kPa. By increasing the overall capillary pressure, through continued testing and process refinement, a tolerable reduction on the order of 1 kPa was obtained.

### 3.2.2 Final Process Plan

With the small samples capable of being held together by sinter alone, and welding having shown to seal the samples without destroying the wick inside, the process plan was then refined for full sized condensers. Adding 22 μm Monel sinter to compensate for shrinkage in both the top and bottom layer during the second sintering step- increased the capillary pressure performance to above the 6 kPa threshold. The process plan is shown in Figure 11(a). The base plates were chemically etched from high-precision 1.25 mm thickness sheet stock, which form 0.75 mm deep trays with 0.5 mm weld flanges. The cavity was filled 0.5 mm up uniformly with 44 μm Monel sinter. The "L" shaped sub-cooling pattern was then added on to the top of the plates in the liquid channel corners, and each half was sintered for 10 mins at 800°C. The 2 mm liquid channel was scribed out along each "L" (shown in Figure 11(b)). The 22 μm layer sinter was added 0.35 mm thick over the subcooling regions of one of the halves, and the other half was pressed face down over the first, and held under compression while the second sintering step was carried out at the same temperature and for the same duration of time as the first step.

Partially assembled condensers, held together by the sinter bridge, were then tested for sufficient capillary pressure, and prepared for welding by filing away any oxide layers formed on the flanges. Local heat applied to weld the flanges together, if unchecked, can cause the condensers to warp. Aluminum heat sinks were machined so that they could tightly sandwich the condenser during the welding process and remove the excess heat absorbed during the process.

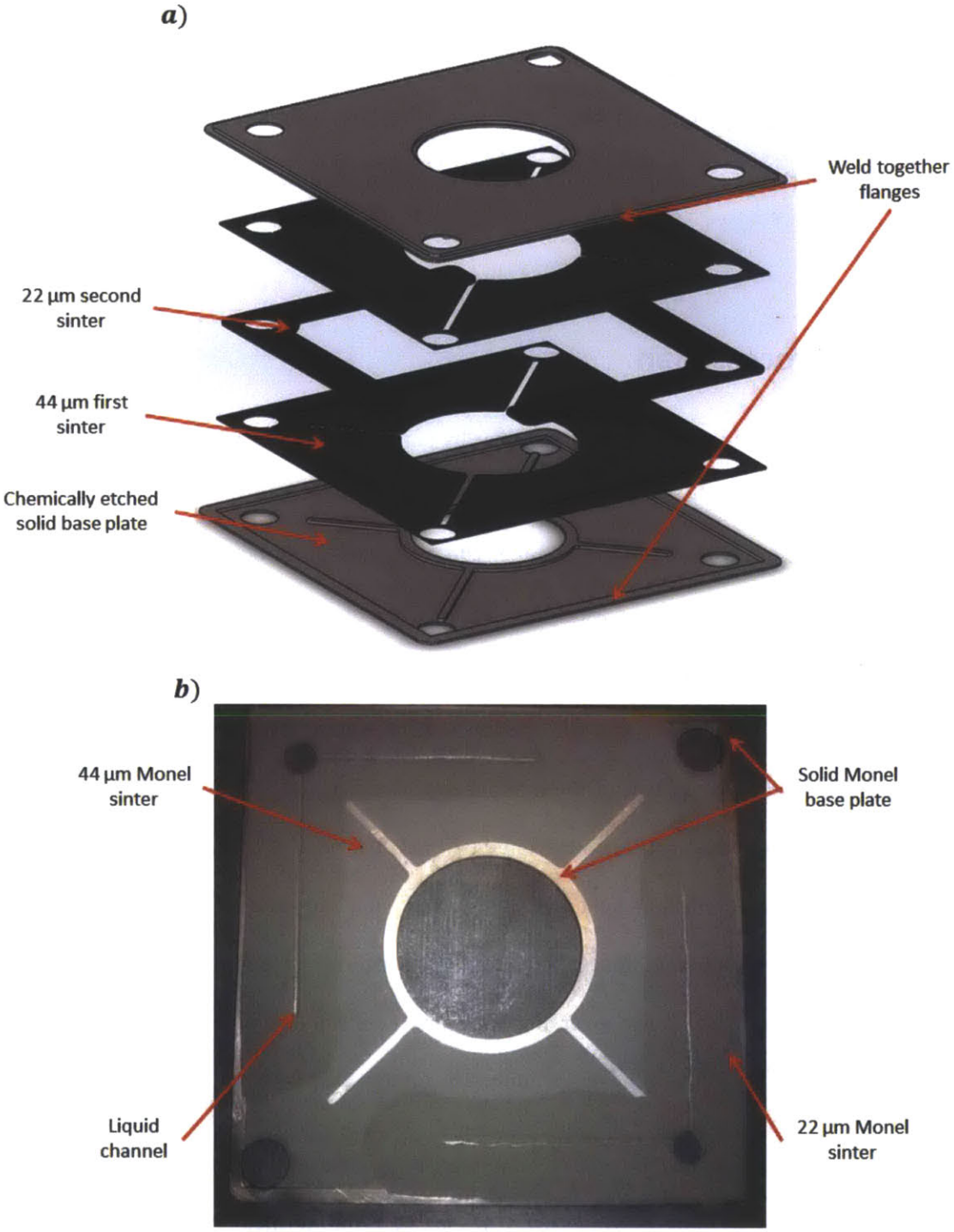


**Figure 11- Process plan for welded condensers**

a) The enlarged view of a welded condenser shows the three integral layers. The solid Monel piece forms a tray in which the structured sinter is created. The 44 µm sinter layer adds the bulk of the wick used within the condenser. The 22 µm sinter addition forms a sinter bridge between the two subcooling lengths, replacing both the solid subcooling plates and the joining braze used previously. (b) The top view of a half-condenser ready for bonding to its other half. Seen here is the two dimensional location of the vapor gap (the lighter gray areas). The only deletive step during this process is the carving of two $2-\mathrm{mm}$ liquid channels at each liquid outlet.

The final welding process introduced a slight reduction in the capillary pressures: $1.7 \pm 0.9$ kPa. However, the capillary pressures of the sinter-bridged condensers were often as high as 13 kPa. Therefore, pressure losses during the welding process were tolerable. The schematic diagram shown in Figure 12 demonstrates the functionality of the condenser, and indicates that very little operational differences were expected when switching manufacturing processes for the condensers. Appendix A provides detailed step-by-step comparison of the two fabrication processes, amended with permission from Hanks [6].

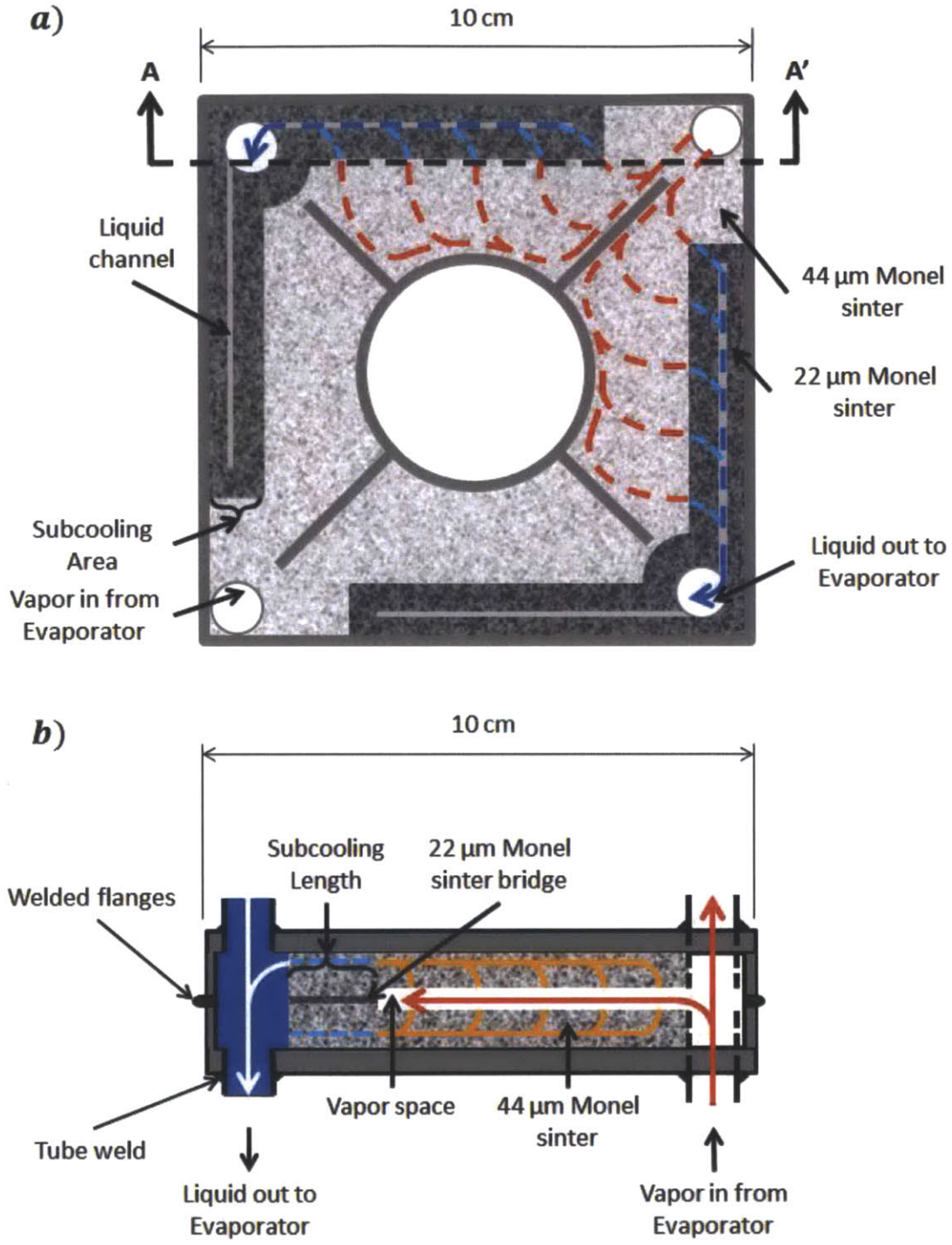


**Figure 12- Schematic diagram of vapor and liquid pathways inside a welded condenser**

(a) Top view of a half-condenser reveals the slightly modified internal structures of a sintered LHP condenser, which shows the carved out liquid channels which transfers subcooled liquid to the outlet at a lower pressure-drop than is expected to occur through sinter. (b) Cross section **AA'** of a welded condenser shows the replacement of subcooling plates with the sinter bridge composed of a less porous sinter. This section is tasked with subcooling the condensed liquid as well as temprarily holding the two half condensers together (not to scale).

# Chapter 4

# Experimental Characterization & Analysis

The aim for this study was to compare the operation of a welded condenser to a brazed condenser, and characterize the performance of the welded condenser under restricted air flow conditions. To characterize the condenser behavior, a custom flow rig designed to regulate the condenser operation independent of an evaporator was used. The condenser was first characterized at a fixed vapor temperature over a range of liquid-side pressures and impeller speeds, and then repeated over different interlayer blockages of the core air flow. Monitoring the pressure changes helped establish a window of safe operation for the condenser, ensuring that neither flooding nor vapor breakthrough to the liquid lines had occurred. Restricting the air flow in the core provided an understanding of impeller design and the effects of unintentional obstructions on an operating condenser, and was used to qualify a previous model.

## 4.1 Single Welded Condenser Experiment

### 4.1.1 Setup & Procedure

The test setup emulated operating conditions of the complete LHP. As shown in Figure 13, the open loop simulator utilized a vapor supply tank to maintain fixed saturation conditions at the condenser inlets (80°C and 47.3 kPa). Steam generated in the vapor tank traveled to the vapor inlets of the condenser, as shown in Figure 14. Within the condenser, vapor occupied the vapor gap. The condenser, sandwiched between a pair of rotating impeller blades driven by a pulse width modulated DC motor, dissipated heat. Above the top impeller was an insulated aluminum plate (not shown) with the same footprint as the condenser. It was used to mimic the effects of having other condensers above it.

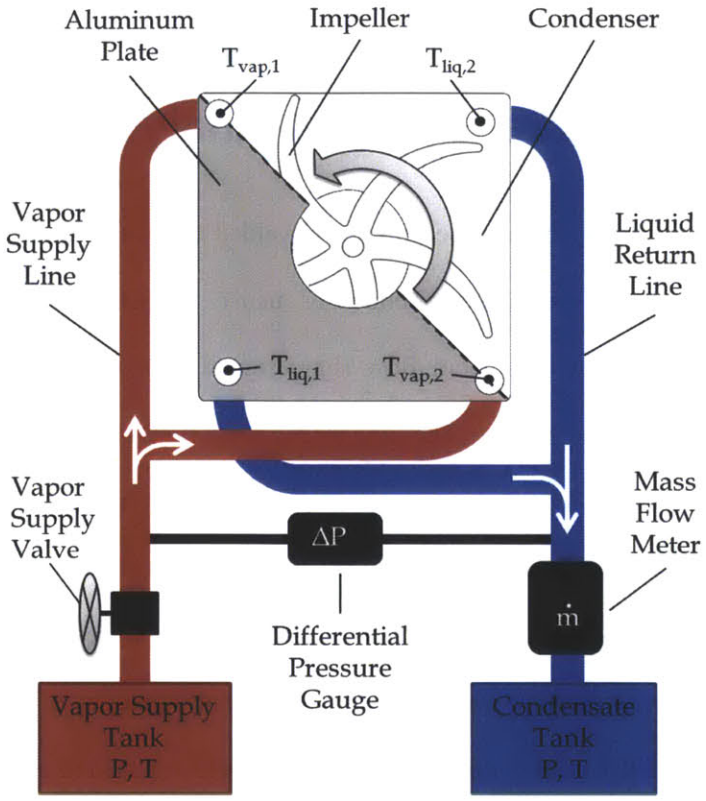


**Figure 13- Schematic diagram of single condenser charaterization setup**

Top-view of an open loop pathway. The working fluid started at the vapor tank where the saturation conditions were fixed at the designed operating temperature for the heat exchanger. It then traveled through the condenser where vapor condensed onto the Monel wick and the shell conducted heat to the impeller- driven air above and below the condenser. The condensate then traveled to a collection tank with saturation fixed in quasi-steady state. The temperature set-point of the liquid tank was slowly lowered, which gradually increased the differential pressure across the inlet and outlet of the condenser until the vapor penetrated the liquid line. (Reproduced with permission from Hanks [6])

Vapor transferred latent heat to the sinter as it reverted back to liquid, and flowed towards the outlet through the sinter. Due to the presence of the wick, the liquid sensibly cooled below saturation in the subcooling length, along its way to the liquid channels where it flowed into another heated tank. This collection reservoir was maintained at a temperature below that of the vapor tank. By incrementally decreasing the temperature of the liquid from the 80°C vapor tank, the pressure difference between the two tanks, and thus across the condenser, was increased until the pressure was large enough to force vapor through the length of the wick without condensation, which represents a breakthrough failure. Pressure at both the inlet and outlet of the condenser were recorded using pressure transducers (PX319,

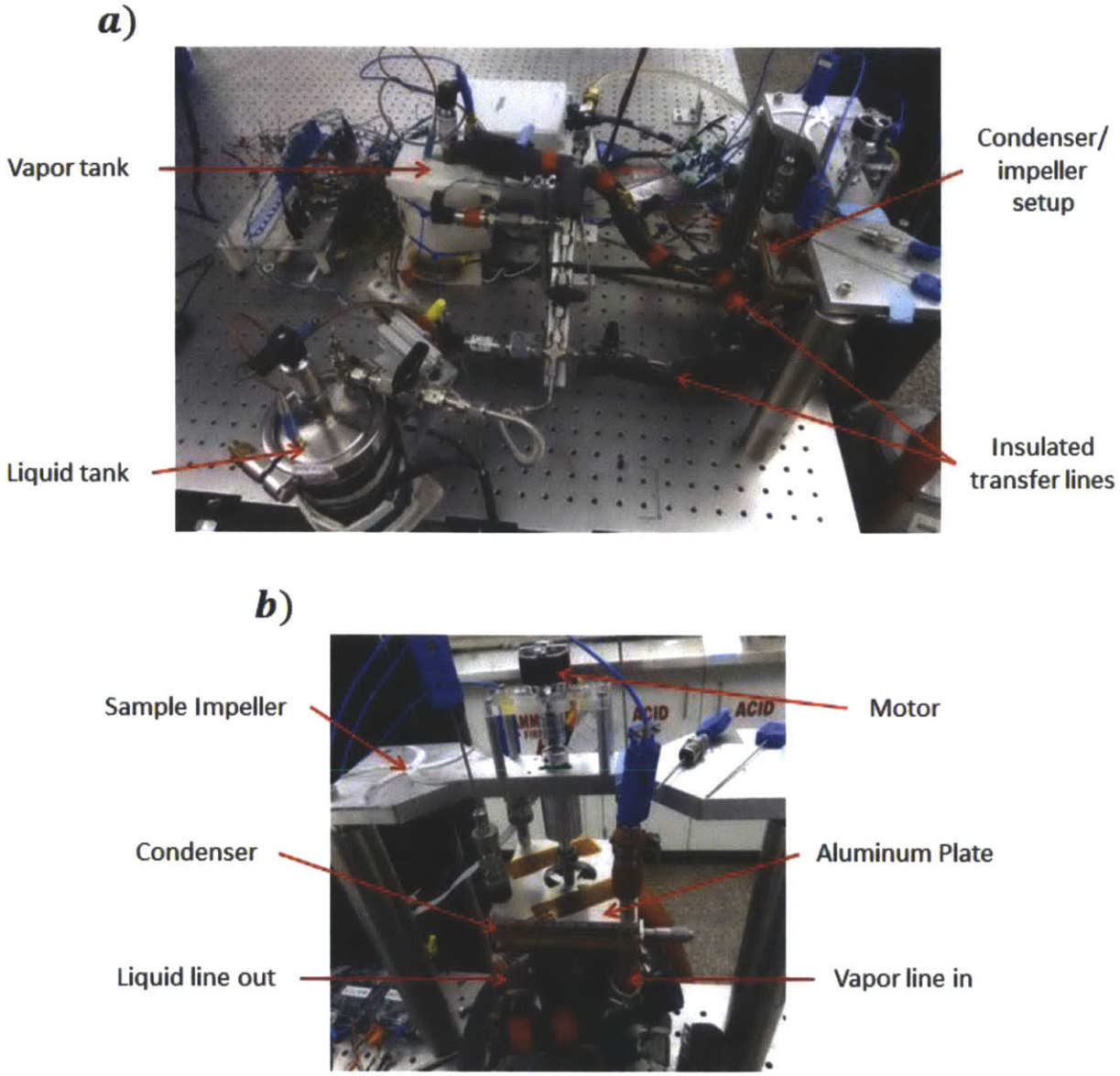


**Figure 14- Single condenser characterization apparatus**

Photographs of the experimental setup demostrate precautions taken to minimize sources of error, including insulating the vapor tank and vapor transport lines and the carefull positioning of the thermocouples (blue probes) used to capture the temperature of the fluid entering and leaving the condenser. The hydrostatic pressure difference, due to the vertical displacement of pressure transducers (metalic cylinders with black wire adapters), was accounted for. (b) The side view of the condenser fixture shows the inlet core of the mock-heat exchanger.

Omegadyne), with $\pm 0.5$ kPa uncertainty. Temperatures of the four inlet/outlet channels and two tanks were recorded using thermocouples (TMQSS-062G-3, Omega) with $\pm 0.5$ °C uncertainty. Labview was used to record the sensor data using a DAQ card (PCI-6289, National Instruments). Power supplied to the band heater was calculated and used to assess heat dissipation performance of the condenser.

Degassed water was used as the working fluid. Non-condensable gases impeded heat transfer by retarding the diffusion of vapor [23]. The water was degassed *in situ*, by freeze-pump-thaw cycling, i.e. freezing water within one of the tanks by submersion in liquid nitrogen, drawing vacuum to remove the gases, and then thawing. The low solubility of gasses in ice allowed non-condensable gases to separate. Thawing and refreezing multiple times ensured that the small amount of gas trapped in the crystalline ice was able to escape.

### 4.1.2 Results

Figure 15 presents experimental results and pressure data as a function of time. Figure 15(a) shows that the steady temperature of the vapor, $T_{vap}$, was just under the 80°C set point. The temperature of the liquid leaving the condenser from both liquid channels is shown in blue, $T_{liq,i}$. The dramatic difference between the two outlet temperatures may be attributed to a large pore diameter pathway that exists partway through the wick near one of the channels subcooling sections.

The liquid outlet saturation temperature $T_{sat,out}$ was determined by converting the saturated vapor inlet temperature to its corresponding saturation pressure, subtracting the measured pressure drop, and then calculating the saturation temperature at this value:

$$T_{sat,out} = T_{sat}\left(P_{sat}\left(T_{vap}\right) - \Delta P\right) \tag{4}$$

Figure 15(a) shows that during the trial, the saturation outlet temperature, $T_{sat,out}$ and the liquid temperatures converged. The trial ended when the temperature of either liquid channel reached the temperature of saturation, which indicated that vapor was traversing the length of the wick, and had broken through. This diminishing temperature difference was the subcooling of the condenser.

$$\Delta T_{subcooling} = T_{sat,out} - \overline{\overline{T_{liq}}} \tag{5}$$

The liquid temperature was averaged over both liquid lines. The subcooling was plotted as a function of pressure drop within the condenser for two runs at differing impeller speeds (Figure 16 (a)). Neither curve reaches $\Delta T_{subcooling} = 0$ °C, which is due to the fact that the two liquid lines had such differing temperatures that the trial was stopped as soon as the first channel showed evidence of vapor penetration. After welding was completed, the measured capillary break-through pressure for this particular condenser was 4.5 kPa. Therefore, its functionality beyond this differential pressure value may appear contradictory. As mentioned earlier, capillary pressure tests were carried out with air, which does not condense. Water vapor on the other hand condenses as it is cooled, which occurs as it comes in contact with the sinter, and flows in contact with liquid water. Hanks had witnessed and characterized the same phenomena in brazed condensers [6].

The welded condenser followed the same three stages of operation as has been seen in brazen condensers. Not much data was collected in the first stage, shown as Zone 1 in Figure 16(a) since according to Hanks this is where the condenser is flooded. This seems likely from the fact that the tanks were at the same saturation point at the beginning of the trial. The cooling provided by the impellers kept the entire condenser flooded with liquid, until a pressure differential can be established

During the next phase of operation, the vapor gap is believed to be entirely filled with vapor and the regions of sinter filled with liquid. Since this is how the condenser was designed to operate, it is referred as the stable operation zone and the meniscus at the phase interface is believed to be stationary. In the final stage, before vapor breakthrough, tendrils of vapor start to travel into the sinter wherever the local pore diameters are greatest. This regime is referred to as the vapor burst mode during which the meniscus recedes towards the liquid channel. This happens at different rates in different places due to the local variation of pore diameters (as seen in Figure 3(b)). The vapor tendrils then cool, and vapor collapses into liquid before reaching the liquid channel. At the very end of a run, the differential pressure is high enough so that vapor traverses the entire singular path of least resistance to the liquid channel port.

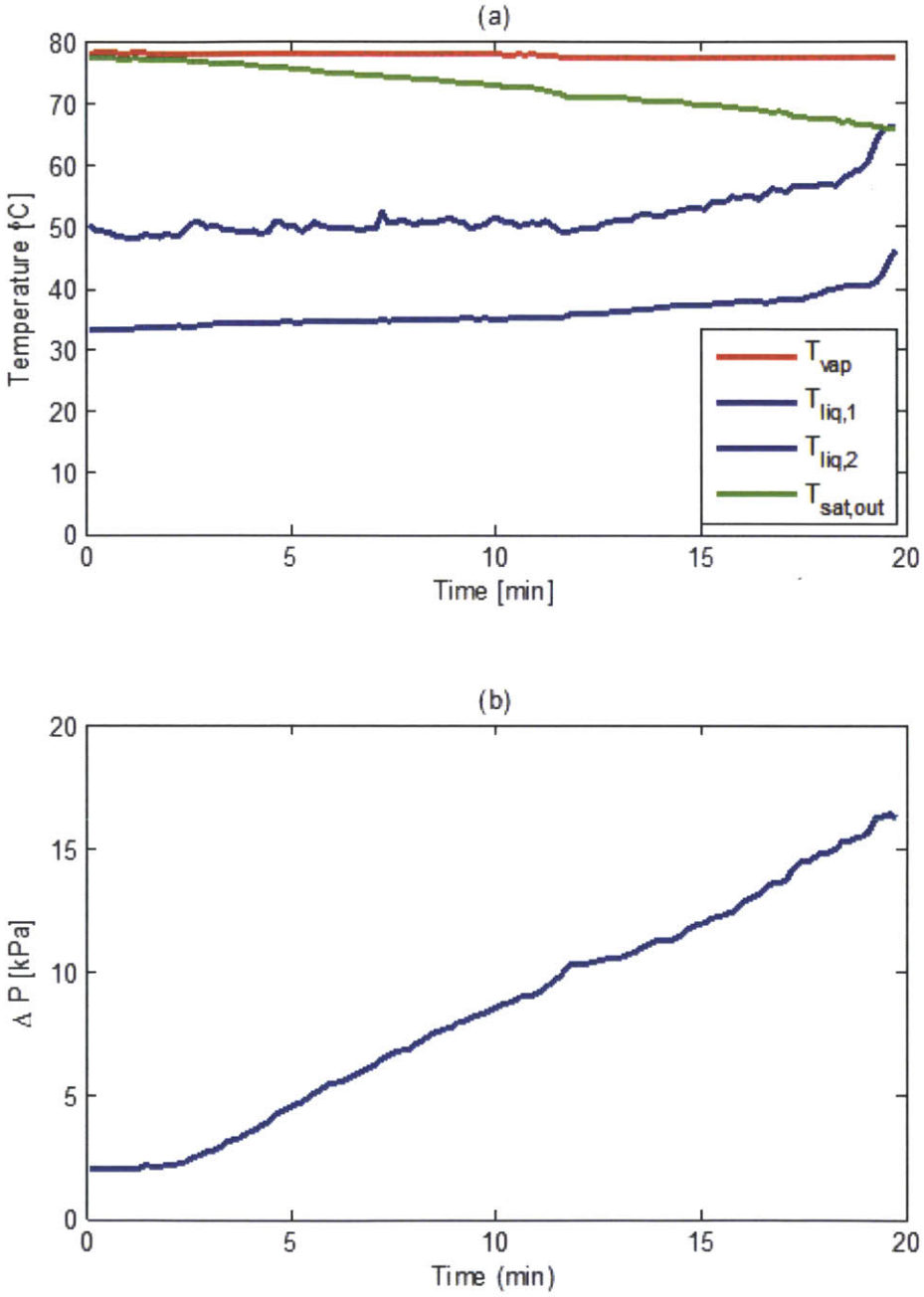


**Figure 15- Single welded condenser operation as a function of time**

(a) Temperature of the liquid exiting the condenser (blue lines) rose to meet the saturation temperature at the outlet (green line). (b) The corresponding differential pressures also showed an increase.

The maximum sustained capillary pressure was 14 kPa for the 2500 RPM case, and 16.5 kPa for the 5500 RPM case. This difference in breakthrough capillary pressure within the same condenser, was due

to increased condensation rate in the higher RPM case, therefore "vapor tendrils" were more likely to collapse and condense until a greater pressure was achieved.

Since temperature and pressures were fixed for the vapor tank, the power supplied to the band heaters in the vapor tank was proportional to the heat being dissipated by the condenser. The heat input into the tank was either lost from the test set up or used to generate saturated steam which condensed into liquid from convective heat dissipation. The band heater power for the two sample impeller speeds has been plotted in Figure 16(b). For the 5500 RPM case there were two stable operating powers at which the condenser power worked, and they correlate to the two zones clearly captured in the subcooling data. The power level for the vapor burst mode was higher than stable mode of operation, due to the fact that there was increased area exposed to vapor which increased condensation. This power increase came at the cost of decreased liquid subcooling because of decreased volume of liquid in the sinter region of the designated subcooling zone.

Unfortunately, not all cases showed such distinction during operations, as shown with the 2500 RPM case (Figure 16). The lack of distinct transition in the power data remains unexplained. This appeared nearly stochastically, and did not trend with either control variable (i.e. power for this study or the blockage ratio in the next section). Figures depicting the single layer characterization for a brazed condenser have been provided in Appendix B for comparison [6].

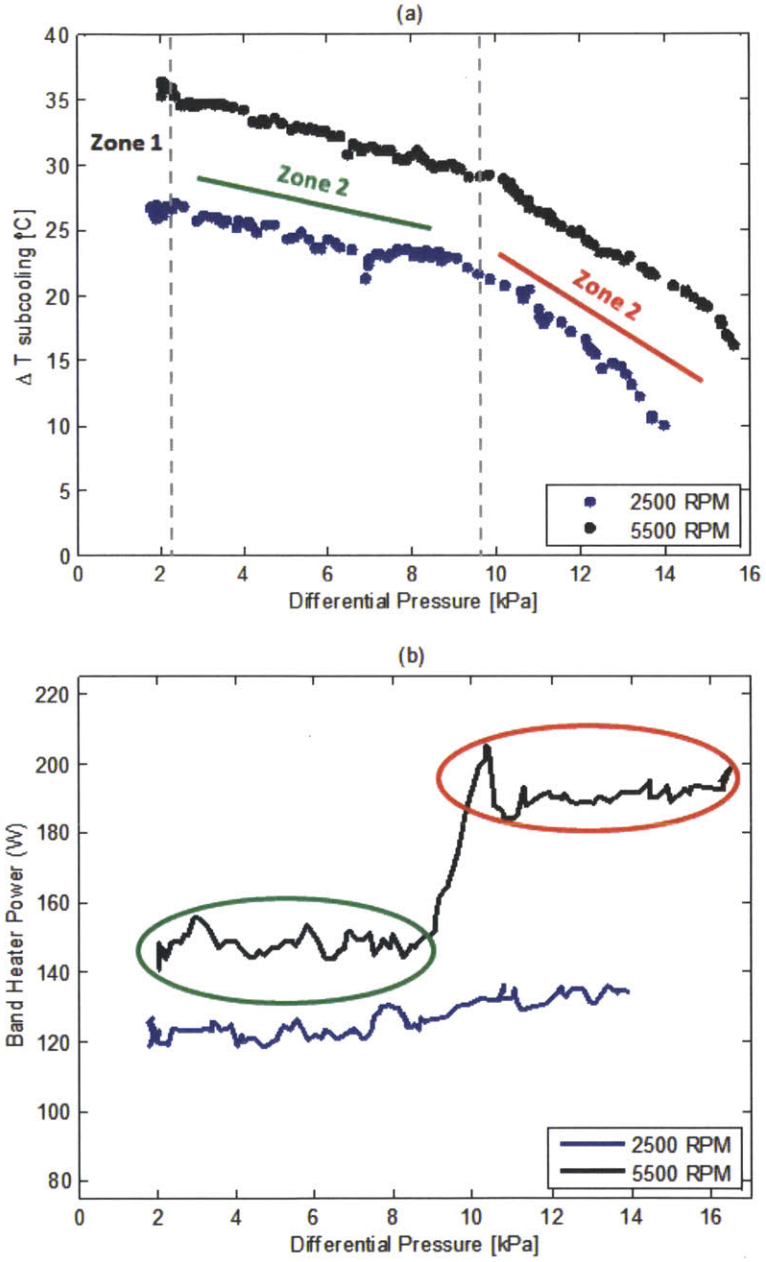


**Figure 16- Welded condenser operation as a function of differential pressure for two impeller speeds.** (a) The liquid subcooling transitioned from a gradual decline to a more rapid decline indicating the two different regimes of operation. The transition occured at a pressure higher than $\Delta P_{cap,max}$ (4.5 kPa) due to the viscous pressure losses and vapor condensation within the sinter. (b) The corresponding heater power sometimes showed the transtion between the two modes.

## 4.2 Simulated Air-flow Restriction

Flow restriction experimentation on a single condenser offers an understanding into how the heat exchanger may perform overall. With only one inlet, the flow rate on different condensers in the heat exchanger is variable, with lower stacks receiving less air flow through its core than condensers closer to the inlet. Analyzing the performance of condensers at various reduced flow rates can be used to predict the performance of a multi-condenser PHUMP. Additionally, previous multi-condenser numerical modeling predicts the heat dissipation of each condenser but not sub-cooling of the condensate leaving the condenser, which is important for determining the stable operating window for the PHUMP.

As seen in Figure 1, the core of the individual condensers allows air to enter from the top, and then radially spread outward. Blocking that area therefore, restricts the flow of air to the condenser and impairs heat dissipation/performance of the condenser. The blockage ratio for the condenser was defined as the fraction of the core area that was occupied by the shaft and impeller blades [13].

$$BR = \frac{\text{Projected area ofthe shaft and impeller blade}}{\text{Area of the condenser core}} \tag{6}$$

In the present study, effects of varying this parameter on the same key metrics analyzed earlier - subcooling and power supplied to the vapor band heater- were determined.

### 4.2.1 Setup & Procedure

The same setup was used as before, with the blockage ratio adjusted by the insulation cover, as shown in Figure 17(a, b). The diameters chosen ranged from the outer diameter of the impeller shaft of 7.9 mm to the inner diameter of the condenser at 40 mm.

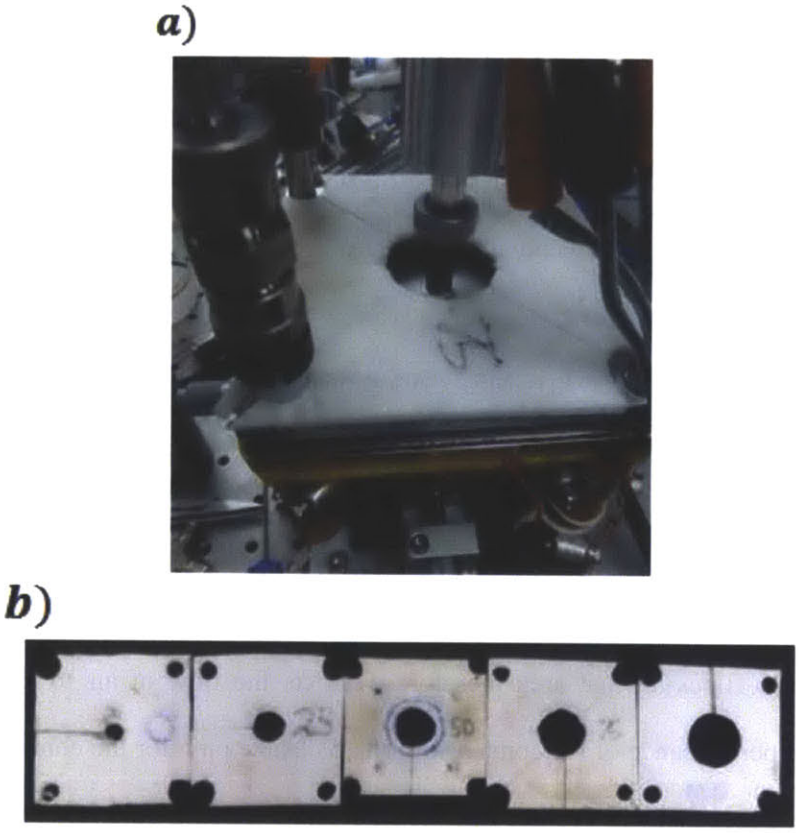


**Figure 17- Single welded condenser setup modification used to test interlayer blockage effects**
The condenser core (a) was covered with different insulator pieces (b) that had varying internal diameters. This alteration was used to define a new inner core diameter. The projected areas of the impellers and the shaft were used to evaluate the blocked area of the core, and yielded unique blockage ratios.

### 4.2.2 Results

As hypothesized, choking down the inlet airflow had a deleterious effect on condenser performance (Figure 18). Going from a blockage ratio near 0 to 1 at 5500 RPM had nearly the same reduction in subcooling and power performance, as reducing the impeller velocity down to 2500 RPM.

The data and linear fit presented in Figure 19 show electrical power applied to the vapor tank band heater in order to maintain it at constant temperature and pressure. The averaged power for each condition was determined from the Band Heater Power vs. Differential pressure plots like the ones

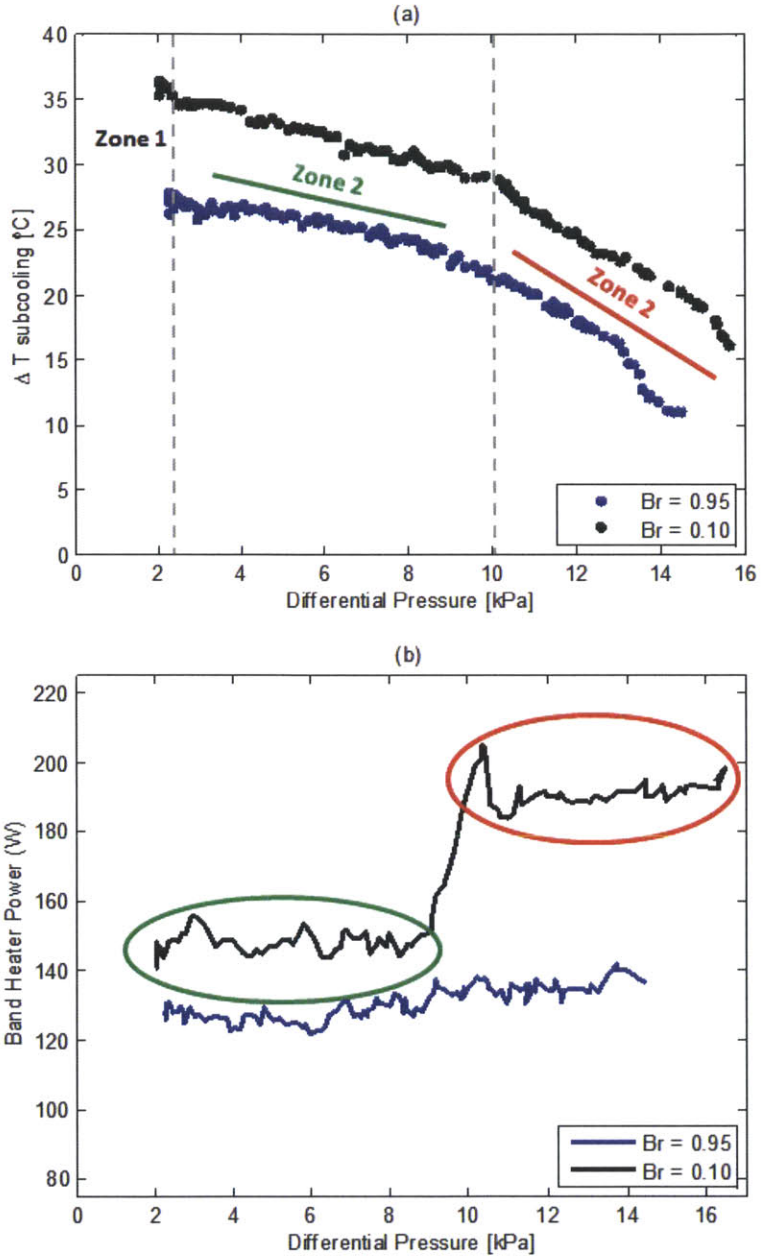


**Figure 18- Welded condenser operation as a function of differential pressure for two blockage ratios**
The effects of increasing the interlayer blockage on the subcooling and band heater power were very similar to the effects of lowering the impeller speed. Both control variables adjusted the external flow heat transfer coefficients that determined the cooling of the condensers. Two operating conditions have been shown, both at 5500 RPM. (a) The subcooling of the liquid was reduced as the access to ambient air at the inlet was reduced (increasing blockage ratio). (b) The power supplied by the vapor heater, a proxy for the heat being dissipated by the condenser decreased as the blockage ratio was increased.

shown in Figure 18 (b). Appendix C provides the derivation of error analysis used for each average power value based on the different uncertainties of the sensors and power supply. When no clear

distinction between stable power and vapor burst power was available, only the averaged final power was used for vapor burst data. Heat loss to the surroundings was approximated from the y-axis intercept of the linear regression for each curve. The linear fit was carried out for each blockage ratio at the first three impeller speeds (2500, 4000, and 5500 RPM). Earlier work has shown that the linear relationship between heat removal and RPM breaks down beyond 5000 RPM [6]. This is due to the fact that the total thermal resistance for dissipated heat, modeled in one dimensional resister network approximation, is the sum of the conductive resistances of the Monel wick and plate, and the convective resistance external to the condenser. Once the impeller speed becomes very high, the conductive resistance cannot be ignored, since it is on the same order of magnitude as the convective resistance.

The plotted stable power and vapor burst pattern (seen in Figure 19 as Zone 2 and Zone 3 respectively), both held to this model, with the 7000 RPM and 9000 RPM band heater power being overpredicted by the linear regression analysis. The effect was further confirmed by the better prediction of power at 9000 RPM for the higher blockage ratios. Although the impeller speed was high, the air restriction reduced the convective heat transfer so the convective resistance was still greater than the conductive resistance. Therefore, the linear regression was more accurate than for the lower blockage ratios, where the convective resistance had not become very small. Another key finding was that y-intercepts differed for the various blockage ratio RPM sweeps and did not entirely converge. The y-intercepts are believed to represent the heat lost from the system and should be constant regardless of flow restriction. The three smallest blockage ratios predicted roughly the same heat loss to the ambient, around 83 W. However, at the higher two blockage ratios, the condenser heat loss was predicted to be 71 W and 47 W.

Finally, the vapor burst heat dissipation rates were calculated by subtracting out the heat loss predictions of the system, shown in Figure 19. Curves for different heat dissipation versus blockage ratios were plotted for three different impeller speeds and normalized by the "unblocked heat dissipation," (shown in Figure 20). The smallest blockage ratio heat dissipation was used as the unblocked heat transfer rate. A curve fit in the form of:

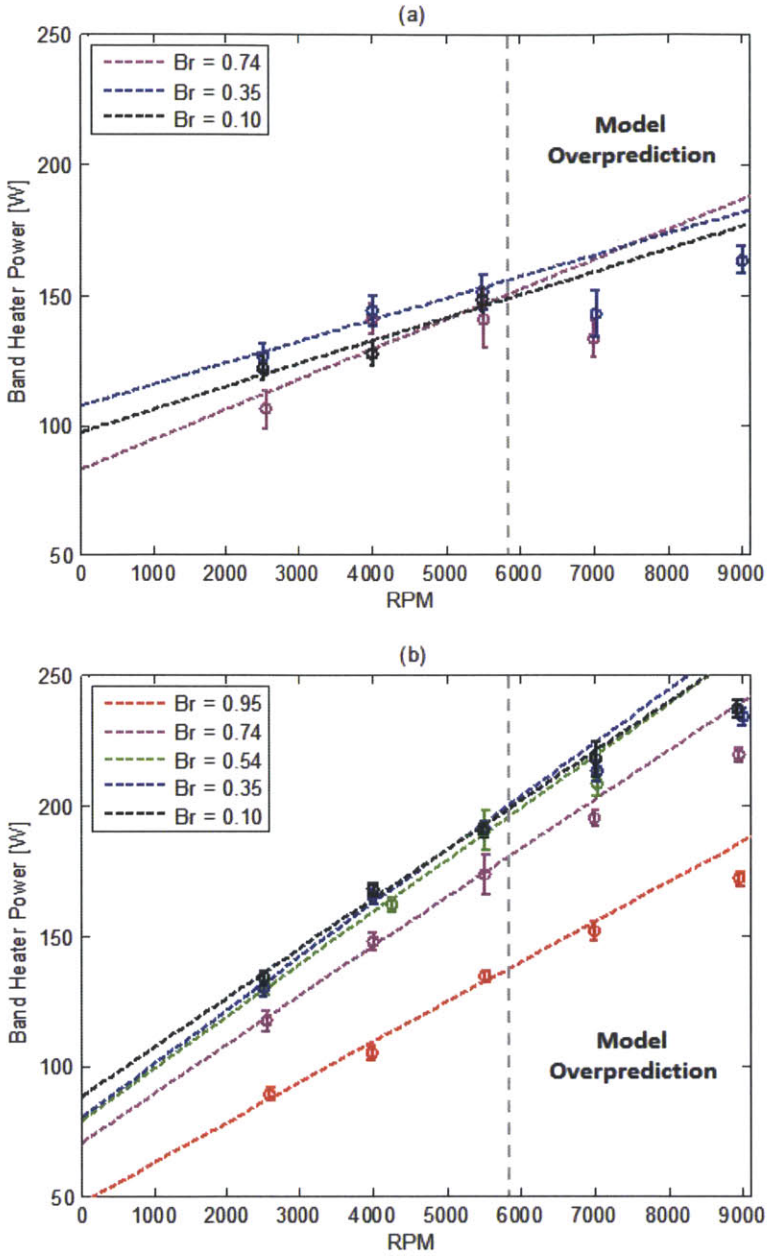


**Figure 19- Supplied vapor heater power as a function of impeller speeds for different blockage ratios**
The band heater power was averaged over the near uniform power operations during (a) stable and (b) vapor burst modes of operation for each trial. When there was no clear stable operation mode, the data point was omitted from (a). The band heater power when plotted against impeller speed had a semi-linear fit that tappered off at very high RPMs. This was explained by a two resistor network model of the heat loss from vapor to ambient air.

$$P^*(BR) = -C_1 e^{C_2} + 1 \tag{7}$$

is also plotted. This form was chosen due to its similar properties to that of the plot generated from a flow network numerical model that was developed by Dr. Wayne Staats as part of his doctoral dissertation. Appendix C includes a reproduction of that plot [13]. The coefficient of determination, $R^2$,

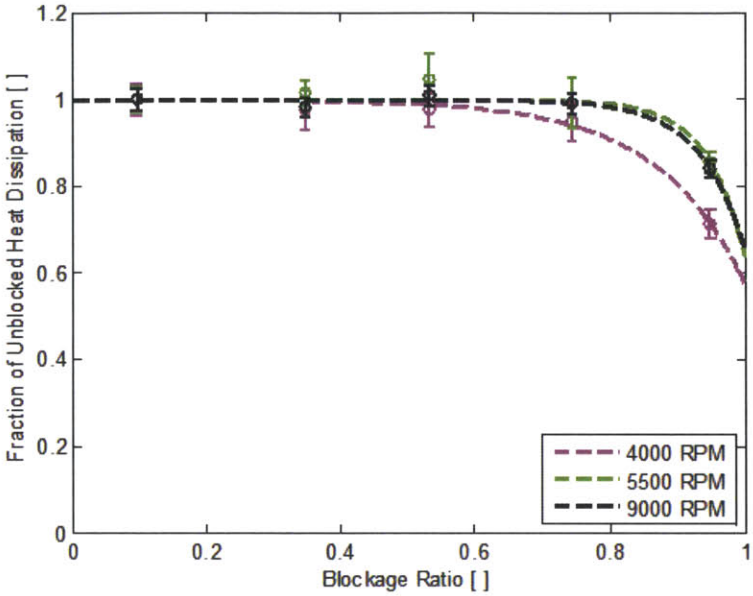


**Figure 20- Fraction of unblocked heat dissipation as a function of blockage ratio**

Heat dissipation from the condenser during vapor burst operation mode, back calculated from the band heater power, was plotted against varying blockage ratios for three different impeller speeds. Each curve was normalized to the lowest blockage ratio (0.1). A functional regression was used to evaluate the general shape of the curve and the predicted performance for a complely blocked condenser.

for this functional regression for the three test cases presented had values over 95%, indicating that the dependence of $P^*$ on the blockage ratio closely follows equation (7).

The key characteristics of the fractional heat transfer curve are: (i) initially as the blockage ratio increased there was very little change in power, (ii) once the blockage ratio had increased sufficiently, performance rapidly deteriorated, and (iii) at complete obstruction of airflow, the core heat dissipation did not cease. Depending somewhat on the impeller speed, the tested condenser showed 60-65% performance for completely blocked inlet; slower impellers had greater blockage effect on performance.

## 4.3 Discussion

The initial study of the condenser verified that switching the manufacturing procedure from brazing to welding did not drastically change the operational performance, and that the regimes previously characterized in brazed condensers also occurred in the welded version. The condenser at lower differential pressures operated in the stable regime where the liquid subcooling decreased only slightly. This region however, did not always appear distinct in the band heater power of the vapor tank or even in the subcooling data. There were many trials where there was no delineation between the stable regime and the vapor burst regime, which should be characterized by a steeper dependence of liquid subcooling at the higher differential pressures.

The difference in the two zones was due to the fact that at the higher differential pressures vapor tendrils penetrate the wick and increase the interface area between the two phases, thus causing a reduction of the subcooling. Although there is a benefit in increasing the heat dissipated from the inherent instability of the formation of vapor tendrils in this zone, it us not advisable to operate in this regime because it may result in vapor collecting in the liquid regime causing cessation of the cycle.

The effect of increasing the impeller speed is similar to that seen in brazed condenser. Increasing the RPM shifted the subcooling curve upward due to increased convective heat transfer. This effect showed some diminishing returns as the conductive resistance through the Monel layers became more dominant. The blockage ratio qualitatively affected performance as previously numerically modeled. Staats however predicted that the effect of complete blockage would be more deleterious, with heat dissipation reduction closer to 60% rather than the 30% found experimentally. A number of factors can account for this. First, the effects of a restriction on multiple condensers, as modeled, may differ from the simulated restriction on an individual condenser. Secondly, the air flow plates adjacent to the condenser were not heated; therefore, the experiment did not mimic the presence of ambient air heating from neighboring condensers. Thirdly, the vapor burst power was utilized due to the ambiguity in much of the data

obtained from the stable operation regime. Using these higher power values would result in a less steep graph when normalizing the results to scale between 0 and 1. Finally, due to the nature of the curve, slight errors in calculating the blockage ratio and/or experimental error can drastically alter the normalized heat dissipation at complete blockage, when extrapolated from experimental values.

The non-convergence of y-intercepts for band heaters power vs. impeller speed for the different blockage ratios brought into question the assumption of whether that y-intercept is actually the heat loss to the ambient air from the system, leaving the remainder of the power defined as the heat dissipated by the condenser. No explanation for the significantly lower y-intercept of the completely restricted airflow is supported by data due to the fact that no change to the system was made. One possibility might be that the high restriction correlates to much slower air velocity jets leaving the condenser impeller apparatus. If these jets are responsible for heat loss of the nearby vapor tank, this velocity reduction could reduce the heat loss experienced by the vapor tank and vapor transfer pipes (see Figure 14(a)). However, since the tank and the transfer pipes were insulated, the heat loss should not be sensitive to changes in air velocity, not on the order of 50% changes in heat losses witnessed in Figure 19(b).

# Chapter 5

# Conclusion & Future Work

## 5.1 Conclusion

Welded condensers were experimentally validated for compatibility with the forced air cooled, loop heat-pipe heat exchanger with multiple sinter lined condensers. The manufacturing process plan for such heat exchanger was developed in this study. The welded condenser characterization confirmed that minor changes within the condenser, namely the replacement of a solid subcooling plate with a porous sinter bridge did not significantly alter key parameters during operation of the condenser. Liquid subcooling and power performances were assessed as a function of differential pressures across the condenser and the velocity of the impeller blades. By back calculating from the heat dissipated by the condenser, the optimal combination of working differential pressure and impeller speed can be obtained for required performance.

Investigating the effects of restricted air-flow into a single condenser core qualitatively validated a numerical model previously conducted, which was used to reconfigure the impeller geometry and mitigate the effect of obstructing the air inlet at the top of the heat exchanger. Additional information generated regarding the liquid subcooling, may be used to determine the cooling performance of the most restricted condenser, whose stable operating range should be used to dictate the operations of the full heat exchanger.

## 5.2 Future work

Future work should be carried out to determine how to extend the use of welding to the assembly of a condenser stack. Preliminary work involving tube joint welds has shown that there will be additional challenges when trying to weld on the face of the condenser - where inlet and outlet tubes are placed, since condenser plates were kept as thin as possible in order to reduce conductive resistance. The use of laser welding should be investigated in order to reduce the heat affected zone and depth of the weld pool.

The lack of a distinguishable stable operating zone needs to be further characterized. Setting up a half condenser test with a transparent, insulating viewing window may help better elucidate how the two zones transition. Similarly, the ability to predict the transition pressure between the modes at varying impeller speeds (or blockage ratios) would yield useful insights and guidelines for operating the PHUMP. This may be done through modeling the characteristic time of travel through the condenser, and the heat loss through the sinter and solid Monel into the air.

# Appendix A-

## Comparison of Manufacturing Process Plans

| Brazing Approach | | |
|---|---|---|
| Step | **Process** | **Description** |
| 1 | Photochemical Etch | Plates are etched from 0.5 mm and 0.75 mm Monel 400 |
| 2 | Silver Braze | Frame plate is bonded to base plate at 970 °C for 12 min in jig for compression and alignment |
| 3 | Sintering | Half-condenser are filled with 44 μm Monel 400 particles (centrifugally packed), scraped to 0.25 mm thin to form vapor space, and sintered at 830 °C |
| 4 | Sintering | 44 pm Monel 400 particles are added to the perimeter of the subcooling section and sintered at 830 °C |
| 5 | Quality Check | Test capillary pressure for each half |
| 6 | AgCu Braze | Two condenser halves are bonded together with eutectic AgCu braze at 810 °C along the edges and between the two subcooling plates |
| 7 | Quality Check | Test sintered and brazed condenser for capillary pressure, and helium leak detect |

**Table 3- Step-by-step fabrication procedure for brazed condensers**

| Welding Approach | | |
|---|---|---|
| Step | **Process** | **Description** |
| 1 | Photochemical Etch | Plates are etched from 1.25 mm Monel 400 to form a tray with weld flanges |
| 2 | Sintering | 0.25 mm layer of 44 μm Monel 400 particles and the subcooling channels are sintered at 800 °C |
| 3 | Sintering | Thin layer of 44 μm Monel power is added to compensate for the shrinkage in step 2 and re-sintered at 800 °C |
| 4 | Sintering | 22 μm Monel 400 particles are added in 0.35 mm layer on top of one of subcooling regions of one plate and the sandwiched under the under. Sinter at 800 °C under compression to bond the two halves |
| 5 | Quality Check | Test capillary pressure for sinter-bridged full condenser |
| 6 | Weld | Outer and inner weld flanges are TIG welded together |
| 7 | Quality Check | Test sintered and welded condenser for capillary pressure, and helium leak detect |

**Table 4- Step-by-step fabrication procedure for welded condensers**

# Appendix B

Reproduced data for comparison to single brazed condenser performance. A characterization of brazed loop heap pipe condensers for single and multi-condenser heat exchangers is described in detail by Hanks [6].

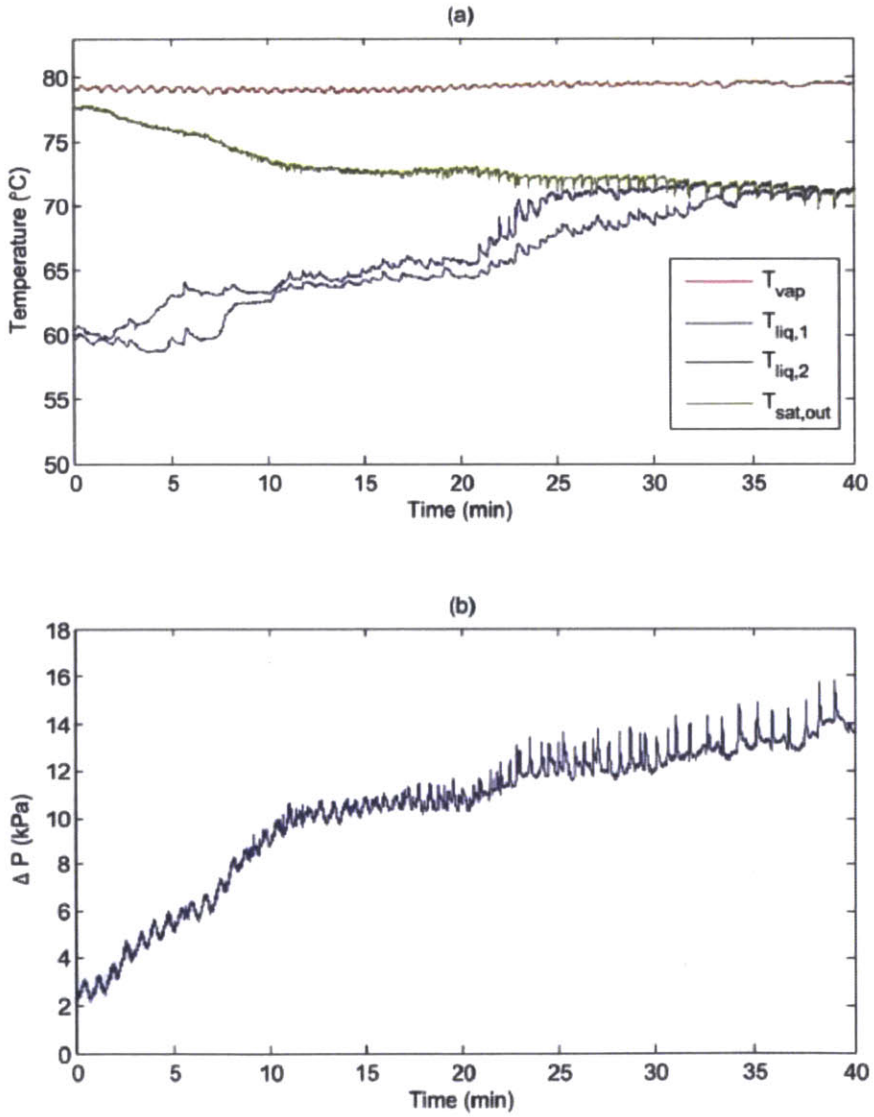


**Figure 21- Results from a single brazed condenser experiment as a function of time**

(a) The temperature of the liquid existing the condenser (blue lines) increased to meet the saturation temperature at the outlet (green line). (b) The corresponding differential pressures also increased (Reproduced with permission from Hanks [6]).

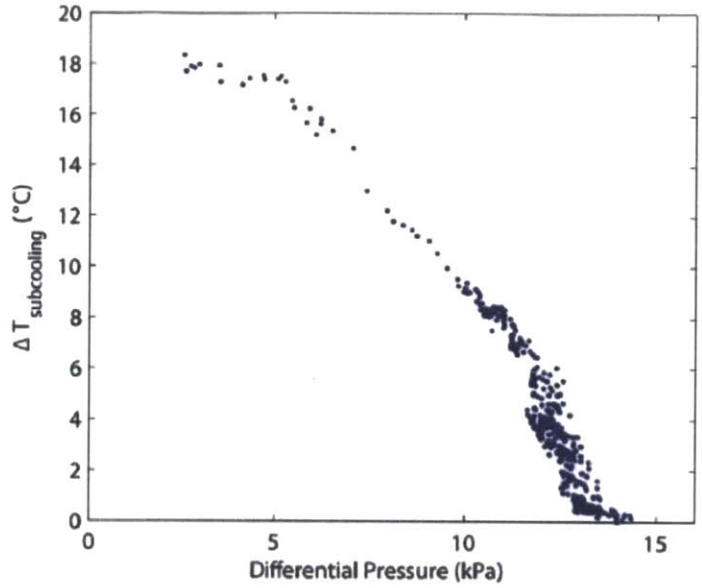


**Figure 22- Changes in liquid subcooling as a function of differential pressure for brazed condensers**
After the breakthrough pressure $\left(\Delta P_{cap,max} = 6.2\ kPa\right)$ was exceeded, the liquid subcooling decreased. (Figure Reproduced with permission from Hanks [6])

Reproduced data for comparison of the effects of interlayer blockage ratio on condenser performance.

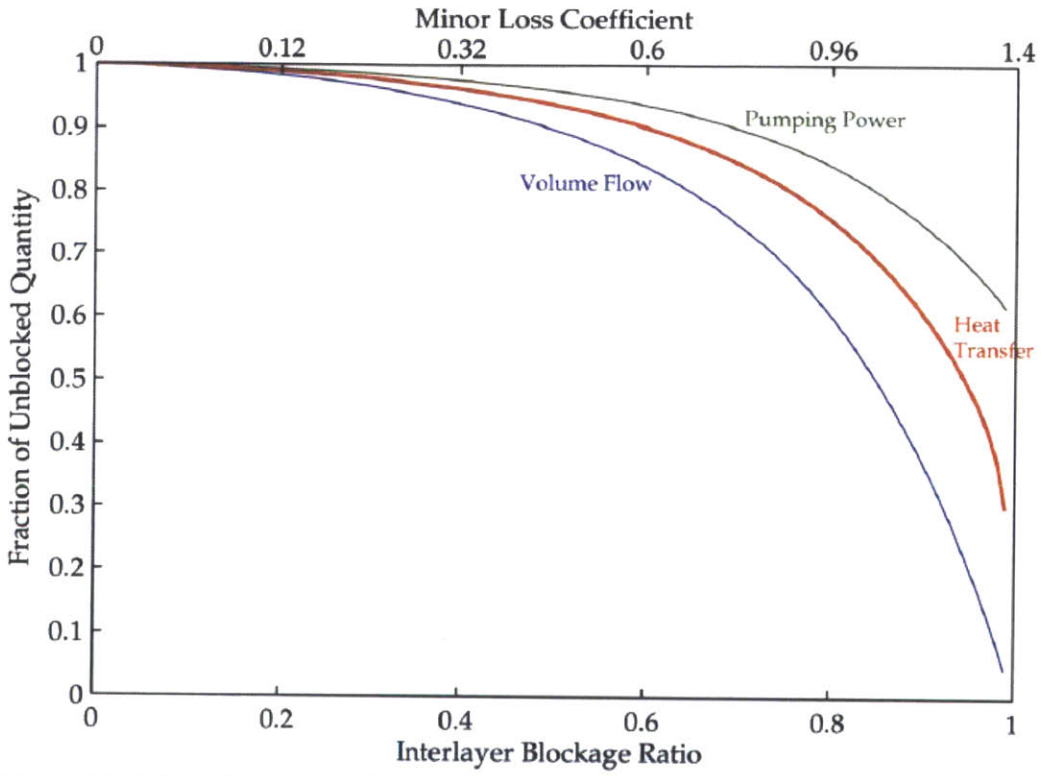


**Figure 23- Effect of interlayer blockage on the performance of a multilayer device**

The interlayer resistance was predicted to significantly reduce the performance of a multilayer device at high blockages. A 6-fan device simulation using a flow circuit model for various interlayer blockage ratios is shown. Of key importance to this study was the heat transfer curve (red line), and the fact that the normalized heat transfer did not go to zero when the inlet was completley blocked. An explanation of this flow circuit model was reported in detail by Staats [13] (reproduced with permission).

# Appendix C

The error bars in the power related figures were calculated using a 95% confidence interval, and accounted for propagated errors from the thermo-couples and the voltage supply.

The experimentally recorded band-heater power was defined as:

$$P_{\text{band heater}} = k[K_{\text{prop}}(T_{\text{set}} - T_{\text{hot}}) + K_{\text{static}}]V^2$$

where:

$k$ – Lumped exprimental constant (unit conversion and band heater resistance)

$K_{\text{prop}}$ – Band Heater proportional constant

$T_{\text{set}}$ – Steam temperature set point

$T_{\text{hot}}$ – Actual steam temeprature

$K_{\text{static}}$ – Band heater static constant

$P_{\text{band heater}}$ – Band heater power

$V$ – Applied band heater volatge

Using known deviations of steady state readings of sensors, and the voltage source,

$\sigma_{T_{\text{hot}}}$ – Thermo couple standard deviation

$\sigma_V$ – Voltage supplier standard deviation

the propagated error deviation was defined as

$\sigma_{P,\text{prop}}$ – Standard deviation of power that is a result of propogated error

$$\sigma_{P,\text{prop}} = \sqrt{\left(\sigma_{T_{\text{hot}}} \frac{\partial P}{\partial T_{\text{hot}}}\right)^2 + \left(\sigma_V \frac{\partial P}{\partial V}\right)^2}$$

where,

$$\frac{\partial P}{\partial T_{hot}} = k\left[-K_{prop}V^2\right]$$

$$\frac{\partial P}{\partial V} = 2kV\left[K_{prop}(T_{set} - T_{hot}) + K_{static}\right]$$

The overall deviation of the heat removal power, using the Pythagorean Theorem, is then:

$$\sigma_{\text{Heat removal}} = \sqrt{\sigma_{P,prop}^2 + \sigma_{P,measured}^2}$$

where

$$\sigma_{P,exp} - \text{ Standard deviation of experimental power}$$

Finally a two tailed 95% confidence interval was used for the power plots:

$$P \pm 1.96\left(\sigma_{\text{Heat removal}}/\sqrt{n}\right)$$

# Bibliography


[1] M. O'Keefe and K. Bennion, "Comparison of hybrid electric vehicle power electronics cooling options," in *Vehicle Power and Propulsion Conference*, Arlington2007.

[2] "EPA Report on Server and Data Center Energy Efficiency," [Online]. Available: http: //www.energystar.gov/index.cfm?c=prod__development.server_efficiency. [Accessed 10 May 2013].

[3] Hewlett-Packard, "Power efficiency and power management in HP Servers," 2012. [Online]. Available: http://h20000.www2.hp.com/bc/docs/support/SupportManual/c03161908/c03161908.pdf. [Accessed 10 May 2013].

[4] A. Ambirajan, A. Adoni, J. S. Vaidya, A. A. Rajendran, D. Kumar and P. Dutta, "Loop heat pipes: a review of fundamentals,," *Heat Transfer Engineering,* vol. 33, no. 4-5, p. 387–405, 2011.

[5] A. S. Shanmuga and R. Velraj, "Thermal management of electronics: A review of literature," *Thermal Science,* vol. 12, no. 2, pp. 5-26, 2008.

[6] D. F. Hanks, Design, fabrication, and characterization of a multi-condenser loop heat pipe, Cambridge: Master's thesis, Massachusetts Institute of Technology, 2012.

[7] "Broad agency announcement: Microtechnologies for air-cooled exchangers (mace)," Technical report, DARPA MTO, 2008.

[8] J. Lustbader, "Air cooling technology for power electronics," U.S. Department of Energy Vehicle Technology Program Annual Merit Review, Golden, 2011.

[9] L. M. Jiji, Heat Transfer Essentials, New York: Begell House, Inc, 2002.

[10] A. Faghri, "Review and advances in heat pipe science and technology," *Journal of Heat Transfer,* vol. 134, December 2012.

[11] D. F. Hanks, T. B. Peters, J. G. Brisson and E. N. Wang, "Characterization of a condenser for a high performance multi-condenser loop heat pipe," in *Proceedings of the ASME 2011 International Mechanical Engineering Congress & Exposition*, Denver, 2011.

[12] T. B. Peters, M. McCarthy, J. Allison, F. A. Dominguez-Espinosa, D. Jenicek, H. A. Kariya, W. L. Staats, J. G. Brisson, J. H. Lang and E. N. Wang, "Design of an integrated loop heat pipe air-cooled heat exchanger for high performance electronics," *IEEE Transactions On Components, Packaging And Manufacturing Technology,* vol. 2, no. 10, pp. 1637-48, 2012.

[13] W. L. Staats, Active heat transfer enhancement in integrated fan heat sinks, Cambridge: Doctorate dissertation, Massachusetts Institute of Technology, 2012.

[14] M. Mcarthy, T. Peters, A. Espinosa, D. Jenicek, A. Kariya, C. Koveal, J. G. Brisson and J. H. Lang, "Design and Analysis of High-Air-cooled Heat Exchanger with an Integratedperformance Capillary-pumped Loop Heat Pipe," in *Proceedings of the 12th IEEE Intersociety Conference on Thermal and Thermomechanical Phenomena in Electronic Systems*, Las Vegas, 2010.

[15] H. A. Kariya, D. F. Hanks, T. B. Peters, J. G. Brisson and E. N. Wang, "Development and characterization of a loop heat pipe with a planar evaporator andcondenser," in *Proceedings of the ASME 2011 International Mechanical Engineering Congress & Exposition*, Denver, 2011.

[16] H. A. Kariya, W. L. Staats, T. B. Peters, M. Cleary, J. G. Brisson and E. N. Wang, "Scaling the Performance of an Air-Cooled Loop Heat Pipe with the Addition of Modular Condensers," in *Proceedings of the 13th IEEE Intersociety Conference on Thermal and Thermomechanical Phenomena in Electronic Systems*, San Diego, 2012.

[17] F. A. Dominguez-Espinosa, "Effect of fabrication parameters on thermophysical," Master's thesis, Massachusetts Institute of Technology, Cambridge, 2011.

[18] C. H. Koveal, Design of parallel plate condensers with sintered wicks for a loop heat pipe, Cambridge: Master's thesis, Massachusetts Institute of Technology, 2010.

[19] H. A. Kariya, Development of an air-cooled, loop-type heat pipe with multiple condensers, Cambridge: Doctorate dissertation, Massachusetts Institute of Technology, 2012.

[20] D. F. Hanks and T. Peters, *Private Communication,* Cambridge, 2012.

[21] E. N. Minkovich, A. D. Shnyrev, V. A. Morgun, A. L. Koresko and O. M. Syvorotko, "Effect of physicochemical processes on gas generation in heat pipes," *Journal of Engineering Physics,* vol. 37, no. 2, pp. 958-61, 1980.

[22] B. Hong, J. T. Zou, X. H. Wang and Z. K. Fan, "Effects of Melting Temperature on Microstructure and Hardness of Silicon Monel Alloy," *Rare Metal Materials and Engineering,* vol. 37, no. 12, pp. 2216-20, 2008.

[23] K. Hijikata, S. J. Chen and C. L. Tien, "Non-condensable gas effect on condensation in a two-phase closed thermosyphon," *International Journal of Heat and Mass Transfer,* vol. 27, no. 8, pp. 1319-25, 1984.

[24] "EPA Report on Server and Data Center Energy Efficiency," [Online]. Available: http: //www.energystar.gov/index.cfm?c=prod_ . [Accessed 10 May 2013].